

# 1 **Size-dependent ice nucleation by airborne particles during dust events** 2 **in the Eastern Mediterranean**

3 Naama Reicher<sup>1</sup>, Carsten Budke<sup>2</sup>, Lukas Eickhoff<sup>2</sup>, Shira Raveh-Rubin<sup>1</sup>, Ifat Kaplan-Ashiri<sup>3</sup>, Thomas  
4 Koop<sup>2</sup> and Yinon Rudich<sup>1\*</sup>

5

6 <sup>1</sup> Department of Earth and Planetary Sciences, Weizmann Institute of Science, 76100 Rehovot, Israel

7 <sup>2</sup> Faculty of Chemistry, Bielefeld University, Universitätsstraße 25, 33615 Bielefeld, Germany

8 <sup>3</sup>Chemical Research Support, The Weizmann Institute of Science, 76100 Rehovot, Israel

9

10 *Correspondence to:* Yinon Rudich (yinon.rudich@weizmann.ac.il)

11 **Abstract.** Prediction of cloud ice formation in climate models remains a challenge, partly due to the complexity of ice-related  
12 processes. Mineral dust is a prominent aerosol in the troposphere and is an important contributor to ice nucleation in mixed  
13 phase clouds, as dust can initiate ice heterogeneously at relatively low supercooling conditions. We characterized the ice  
14 nucleation properties of size-segregated mineral dust sampled during dust events in the Eastern Mediterranean. The sampling  
15 site allowed to compare between the properties of airborne dust from several sources with diverse mineralogy that passed over  
16 different atmospheric paths. We focused on particles with six size-classes, determined by the Micro-Orifice Uniform Deposit  
17 Impactor (MOUDI) cut-off sizes: 5.6, 3.2, 1.8, 1.0, 0.6 and 0.3  $\mu\text{m}$ . Ice nucleation experiments were conducted in the  
18 Weizmann Supercooled Droplets Observation on Microarray (WISDOM) setup, where the particles are immersed in nanoliter  
19 droplets using a microfluidics technique. We observed that the activity of airborne particles depended on their size-class, where  
20 supermicron and submicron particles had different activities, possibly due to different composition. The concentrations of ice  
21 nucleating particles and the density of active sites ( $n_s$ ) increased with the particle size and particles concentration. The  
22 supermicron particles in different dust events showed similar activity, which may indicate that freezing was dominated by  
23 common mineralogical components. Combining recent data of airborne mineral dust, we show that current predictions, which  
24 are based on natural dust or standard mineral dust, overestimate the activity of airborne dust, especially for the submicron  
25 class, and therefore we suggest to include information of particle size in order to increase the accuracy of ice formation  
26 modelling and, thus, in weather and climate predictions.

## 27 **1 Introduction**

28 Cloud droplets can supercool to 238 K before homogeneous freezing occurs (Koop and Murray, 2016; Rosenfeld and Woodley,  
29 2000). At warmer temperatures, heterogeneous ice nucleation (HIN), where the presence of aerosol particles lowers the  
30 required energy barrier to form a stable ice nucleus is the common pathway of ice formation (Murray et al., 2012; Pruppacher

31 and Klett, 1997;Khvorostyanov and Curry, 2004;Hoose and Möhler, 2012). These ice-nucleating particles (INPs) can be  
32 activated at sub-zero temperatures and subsequently lower humidity conditions, mainly by interaction with supercooled  
33 droplets. INPs are relatively rare particles and comprise only about  $10^{-5}$  of the total ambient particles in the free troposphere  
34 (Rogers et al., 1998). Yet, their interaction with clouds can greatly influence climate (Gettelman et al., 2012;Tan et al.,  
35 2016;Lohmann and Feichter, 2005). Therefore it is important to represent them well in weather and climate models (DeMott  
36 et al., 2010). Currently, ice formation is a source of great uncertainty in cloud and climate models, partly due to the complexity  
37 of ice processes and the insufficient understanding of the key surface properties which determine an INP (IPCC, 2013). To  
38 improve the predictions of models, a great effort is invested in the characterization of INPs and in the development of  
39 parametrizations based on their physical and chemical properties (Cantrell and Heymsfield, 2005;Niemand et al., 2012;Ullrich  
40 et al., 2017).

41 One of the most abundant INP in the atmosphere is mineral dust, which originates in dryland zones, such as deserts (Middleton,  
42 2017;DeMott et al., 2003b). Field observations have identified an increase in INP concentrations and ice clouds formation in  
43 the presence of mineral dust (Ansmann et al., 2008;Rosenfeld et al., 2001;DeMott et al., 2003b;Cziczo et al., 2004;Sassen et  
44 al., 2003). Ice residuals often contain mineral particles (Cziczo et al., 2013;Cziczo and Froyd, 2014;Twohy and Poellot, 2005).  
45 Mineral dust has high spatial and temporal variability, impacting atmospheric, oceanic, biological, terrestrial and human  
46 systems (Garrison et al., 2003;Gat et al., 2017;Jickells et al., 2005;Mahowald et al., 2014;Mazar et al., 2016;Middleton and  
47 Goudie, 2001). Each year, gigatonnes of dust are transported globally over long distances, dominating the atmospheric aerosol  
48 mass and aerosol optical depth (AOD) (Chiapello et al., 1999;Tegen and Fung, 1994;Ben-Ami et al., 2010;Prospero,  
49 1999;Koren et al., 2006). Though the exact property of an aerosol that determines its ice nucleation ability remains unclear, it  
50 was consistently shown that the mineral composition plays an important role (Kanji et al., 2017), and that for a certain mineral  
51 type, larger particles are more effective heterogeneous INP than the small ones (Archuleta et al., 2005;Lüönd et al., 2010;Welti  
52 et al., 2019). Local surface features such as steps, cracks and cavities, a close match of the surface lattice with that of ice, or  
53 surface hydroxyl groups (Freedman, 2015;Marcolli, 2014;Zielke et al., 2015;Kiselev et al., 2017;Fletcher, 1969;Tunega et al.,  
54 2004;Anderson and Hallett, 1976;Pruppacher and Klett, 1997) are believed to be the responsible factors for the ice nucleation  
55 ability of mineral surfaces.

56 Natural mineral dust particles are often chemically similar but differ in their mineralogy (Engelbrecht et al., 2009), and the  
57 particles are often composed of a mixture of minerals (internally mixed), such as clays, quartz, feldspars and calcites (Claquin  
58 et al., 1999). Other common minerals are palygorskite, hematite, halite, gypsum, gibbsite and goethite (Ganor et al.,  
59 1991;Perlwitz et al., 2015;Kandler et al., 2007;Mahowald et al., 2014). The mineralogy of mineral dust is set by its source  
60 region and is considered to be an important factor that determines its freezing characteristics (Zimmermann et al.,  
61 2008;Augustin-Bauditz et al., 2014). Traditionally, clay minerals were thought to be responsible for atmospheric ice nucleation  
62 because they compose much of the dust fraction. However, using standard mineral particles, Atkinson et al. (2013) showed  
63 that K-feldspar is the most efficient type, and suggested that it could dominate atmospheric ice formation at relatively high

64 temperatures, above 258 K. This was further supported by measurements of natural mineral dust from desert surfaces  
65 worldwide, where the importance of quartz mineral was also indicated (Boose et al., 2016b).

66 Airborne mineral dust (AMD) can experience chemical and physical modifications during its atmospheric transport that may  
67 alter dust's ability to nucleate ice (Kanji et al., 2013). It was shown that atmospheric aging processes can change the size, the  
68 morphology and the surface chemistry of the particles. For example, adsorption of organic components on AMD (Murphy et  
69 al., 2006; DeMott et al., 2003a; Falkovich et al., 2004) or coatings of nitrates, chlorides and sulphates which enhance the  
70 hygroscopicity of the particles (Krueger et al., 2004; Laskin et al., 2005; Li and Shao, 2009). Levin et al. (1996) found that  
71 AMD particles transported over the Mediterranean Sea were often coated with sulphate and other soluble materials, which  
72 affect clouds' microphysical properties and can eventually result in enhanced ice nucleation. In addition, mineral dust carries  
73 biological components, such as bacteria and fungi, which are known to have the ability to induce ice nucleation at relatively  
74 high temperatures (Gat et al., 2017; Mazar et al., 2016; Pratt et al., 2009; O'Sullivan et al., 2016). Further modifications that can  
75 occur during AMD atmospheric transport are the differentiation of size and mineralogy. These can occur due to gravitational  
76 sedimentation, for example, where larger particles sediment faster than the smaller ones. Near source regions, dust samples  
77 were richer in components that are more abundant in the coarse fractions, such as quartz and potassium feldspars, while in  
78 remote locations, higher amount of clay minerals and sodium/calcium feldspar were observed (Murray et al., 2012; Schepanski,  
79 2018).

80 While there are only few measurements of AMD close to source regions (Price et al., 2018; Boose et al., 2016a; Ardon-Dryer  
81 and Levin, 2014; Schrod et al., 2017), parameterizations of ice formation in climate models are often based on the freezing  
82 properties of natural dust or soil samples collected from deserts or standard dust particles (Niemand et al., 2012; Connolly et  
83 al., 2009; Ullrich et al., 2017; Atkinson et al., 2013; Broadley et al., 2012), that may not sufficiently represent AMD (Boose et  
84 al., 2016b; Spichtinger and Cziezo, 2010). Natural dust samples showed higher ice nucleation ability than AMD samples,  
85 possibly due to atmospheric processing of AMD that may lead to deactivation, and possibly due to laboratory processes, such  
86 as milling or sieving, that were applied to the natural dust samples and may have enhanced its activity (Boose et al., 2016b).

87 In this study, we sampled airborne particles during dust events in the Eastern Mediterranean and investigated their ice  
88 nucleation abilities. The Eastern Mediterranean is located in the strip of the world's main deserts, and experiences transport of  
89 desert dust from different sources. The main source is the Sahara Desert in North Africa. It is estimated that about 100 million  
90 tons of dust per year is lifted from the Sahara towards the Eastern Mediterranean, during late winter and spring (Ganor,  
91 1994; Ganor and Mamane, 1982; Ganor et al., 2010). In autumn, local dust is transported, commonly from the Arabian Peninsula  
92 and the Syrian Desert (Dayan et al., 1991; Ganor, 1994). The dust events are often associated with the regional Eastern  
93 Mediterranean synoptic systems, such as winter lows and Red-Sea troughs (Ganor et al., 2010). Our sampling site was located  
94 in Israel, where Saharan dust is transported over North Africa and/or the Mediterranean Sea, and Syrian and Arabian dust is  
95 transported over land from the east (Ganor et al., 1991). These distinct sources and paths allow investigating the ice nucleation  
96 properties of AMD with diverse origins and transport paths.

97 The ability of the collected particles to initiate immersion freezing was studied using the Weizmann Supercooled Droplets  
98 Observation on a Microarray (WISDOM) instrument (Reicher et al., 2018), and one of the dust events was studied using the  
99 Bielefeld Ice Nucleation ARraY (BINARY) instrument (Budke and Koop, 2015). We characterized the concentrations and the  
100 density of ice nucleation active sites (INAS) of AMD in different size-classes for several dust cases, as well as combined recent  
101 literature and available AMD data to understand how well AMD is represented in models based on recent parameterizations.  
102

## 103 **2 Data and Methods**

### 104 **2.1 Sampling**

105 Airborne particles were sampled during six dust events in 2016 and 2017, detailed in Table 1. Sampling started when the  
106 visibility reduced due to increasing concentrations of particulate matter (PM). The sampling site is located on a roof of a three-  
107 story building in Rehovot, Israel (31.9N, 34.8E about 80m AMSL). The location is often impacted by mineral dust storms,  
108 transported from nearby and distant geographical locations, mainly from the Sahara and Arabia deserts, and less frequently  
109 from the Syrian Desert, depending on the season and the synoptic conditions (Dayan, 1986;Ganor et al., 2010;Kalderon-Asael  
110 et al., 2009).

111 Particles were collected on polycarbonate filters (47mm cyclopore, 0.1  $\mu\text{m}$  isopores; Whatmann), using the Micro-Orifice  
112 Uniform Deposit Impactor (MOUDI) (model 110-R). The MOUDI is a 10-stage impactor with 18  $\mu\text{m}$  cut-point inlet stage  
113 followed by size segregating stages with cut points ( $D_{50}$ ) between 0.056 and 10  $\mu\text{m}$  in aerodynamic diameter (Marple et al.,  
114 1991). The particles are collected on the different stages as function of their aerodynamic diameter. The collection efficiency  
115 for each particle size is described in Marple et al. (1991). Sampling time ranged between 17 and 48 h with a 30 L  $\text{min}^{-1}$  sample  
116 flow rate, similarly to previous studies (Huffman et al., 2013;Mason et al., 2015).

### 117 **2.2 Air mass Back Trajectories**

118 Back trajectories were calculated by a Lagrangian method, using LAGRANTO 2.0 (Sprenger and Wernli, 2015). The  
119 calculation of air mass trajectories was based on wind data from the European Centre for Medium-Range Weather Forecasts  
120 ERA-Interim reanalysis (Dee et al., 2011), available every 6 h, at  $1^\circ \times 1^\circ$  horizontal grid and 60 vertical hybrid levels. For each  
121 6-h time step during each event, 72 h back trajectories were calculated, from all available data grid points with pressure larger  
122 than 850 hPa, resulting in 11 trajectories, which end their path in the lower troposphere for each calculation. In a second step,  
123 the Eulerian densities of the resulting trajectories were computed by gridding the trajectories for each event, smoothed by using  
124 a radius of 100 km and interpolated to 1 h. Finally, the trajectory density was summed over the entire event duration and  
125 normalized by the maximum trajectory count.



## 126 **2.3 Dust Column Mass Density Maps**

127 Time averaged maps of dust column mass density (hourly  $0.5^\circ \times 0.625^\circ$ ) reanalysis data were obtained from the Modern-Era  
128 Retrospective analysis for Research and Applications (MERRA-2). Maps were produced using NASA's Global Modeling and  
129 Assimilation Office (GMAO) (Gelaro et al., 2017), for a period of up to 72 h prior to the sampled event.

## 130 **2.4 Particulate Matter Data**

131 Particulate matter mass data were obtained from the Israeli Ministry of Environment website. Concentrations of particles with  
132 aerodynamic diameters smaller than  $10 \mu\text{m}$  ( $\text{PM}_{10}$ ) were measured in the Rehovot station, located about 1 km from our  
133 sampling site. The 5-minutes mean data was used to calculate peak and mean concentrations of the sampled dust events.

## 134 **2.5 Particle Number-Size and Surface Area distributions**

135 Particle size distribution and concentrations between  $0.25$  and  $32 \mu\text{m}$  was measured on site by an optical particle counter (OPC;  
136 GRIMM Technologies model 1.109), in parallel to the MOUDI sampling. In order to estimate the total surface area that was  
137 collected on the different stages, we assumed that the particles are spheres and used the diameter of the GRIMM midpoint of  
138 the different GRIMM's channels as the particles' diameter.

## 139 **2.6 Conversion of GRIMM channels to MOUDI stages**

140 To determine the total surface area collected on MOUDI's filter, a conversion matrix between the GRIMM channels and the  
141 MOUDI stages was applied. The conversion was based on the particle collection efficiency curves of the MOUDI and inter-  
142 stage particle losses reported in Marple et al. (1991). Figure 1 demonstrates the fraction of particles that are collected on the  
143 stages based on their aerodynamic diameter. Freezing analyses focused on stage #2 ( $D_{50} = 5.6 \mu\text{m}$ ), stage #3 ( $D_{50} = 3.2 \mu\text{m}$ ),  
144 stage #4 ( $D_{50} = 1.8 \mu\text{m}$ ), stage #5 ( $D_{50} = 1.0 \mu\text{m}$ ), stage #6 ( $D_{50} = 0.6 \mu\text{m}$ ) and stage #7 ( $D_{50} = 0.3 \mu\text{m}$ ). For example, most of  
145 the particles with an optical diameter  $> 8.5 \mu\text{m}$  will be collected on stage #2 ( $D_{50}=5.6 \mu\text{m}$ ), whereas all the particles with an  
146 optical diameter  $> 17.5 \mu\text{m}$  are assumed to be collected on former stages (inlet and stage #1). In some cases, particles in a  
147 certain size are likely to impact on two different MOUDI stages. For example, a small fraction of particles with  $0.5 \mu\text{m}$  optical  
148 diameter are collected on stage #5 ( $D_{50}=0.6 \mu\text{m}$ ), and most of them impact on stage #6 ( $D_{50}=0.3 \mu\text{m}$ ). The initial particle  
149 concentration that was used is the accumulated sum of all particles for the entire sampling period.

## 150 **2.7 Ice Freezing Experiments and Quantification**

### 151 **2.7.1 WISDOM**

152 Immersion freezing activity of the sampled ambient mineral dust was measured using suspensions of the collected particles  
153 that were extracted from the filters by dry sonication (VialTweeter, model UP200St; Hielcher). This type of sonication method  
154 is more effective than the ultrasonic bath in which most of the energy is dissipates in the surrounding water. A quarter filter

155 was inserted into a 1.5 ml Eppendorf vial with 0.3 ml deionized water, and sonicated in three 30 s cycles, to avoid heating  
 156 produced during intense sonication. The suspension was immediately used for droplet production and freezing experiments in  
 157 WISDOM as detailed in Reicher et al. (2018). Briefly, an array of 0.5 nL monodispersed droplets (~100  $\mu\text{m}$  diameter,  
 158 suspended in an oil mixture) was generated in a microfluidic device that was cooled by a commercial cooling stage (THMS600,  
 159 Linkam) under a microscope (BX-51 with 10X magnification, Olympus) coupled to a CCD camera. The device was first  
 160 cooled at a faster constant rate of 10  $\text{K min}^{-1}$  from room temperature to 263 K, since freezing events were not expected and  
 161 indeed were never observed in that temperature range. Then a constant cooling rate of 1  $\text{K min}^{-1}$  was used until all the droplets  
 162 froze. The temperature uncertainty was  $\pm 0.3$  K, based on error propagation between the calibrated droplet temperature and  
 163 the uncertainty of the temperature sensor that is located in the cooling stage (see Reicher et al. (2018) for more details).

## 164 2.7.2 BINARY

165 The Bielefeld Ice Nucleation ARraY (BINARY) is an optical freezing array of droplets pipetted on a hydrophobic substrate in  
 166 separated sealed compartments and cooled in a Linkam cooling stage (LTS120) (Budke and Koop, 2015). In the present study  
 167 an array of 64 droplets of 0.6  $\mu\text{L}$  was employed. Suspensions were prepared by extracting a quarter filter in 1.5 ml of double-  
 168 distilled water (that is, 5 times more diluted than WISDOM suspensions), using a bath sonicator (Elma Transsonic Digital, TP  
 169 670/H) for 30 min. The bath temperature increased during sonication from about 288 to 308 K. The obtained suspensions  
 170 were used directly and further diluted (1:10) for another set of measurements with reduced surface area of the particles in the  
 171 droplets. For the freezing experiments, the droplets were cooled at a rate of 1  $\text{K min}^{-1}$ . Temperature uncertainty was  $\pm 0.3$  K.

## 172 2.7.3 Quantification of Freezing Properties

173 The cumulative concentration of INP present in a volume of solvent,  $V$ , at temperature  $T$ , was derived using the fraction of  
 174 frozen droplets ( $f_{ice}(T)$ ), that was obtained directly from the freezing experiments (Vali, 1971):

$$175 \quad K(T) = \frac{-\ln(1-f_{ice}(T))}{V} \quad [\text{cm}^{-3} \text{ of water}] \quad (1).$$

176 For control experiments, a quarter of blank filter was immersed in pure water, similarly to freezing experiments of the  
 177 airborne samples, and the concentration of the background impurities ( $K_{imp}(T)$ ) were subtracted from the concentrations that  
 178 were detected for airborne samples.

179 The atmospheric concentrations of INP per unit volume of air as a function of temperature,  $INP(T)$ , were determined by  
 180 incorporating the sampling and solvent parameters into Eq. 2 (Hader et al., 2014):

$$181 \quad INP(T) = \left( K(T) - K_{imp}(T) \right) \frac{V_{solvent}}{f \cdot V_{air}} \quad [\text{L}^{-1} \text{ air}] \quad (2),$$

182

183 where  $V_{solvent}$  is the volume of the water used for extraction,  $V_{air}$  is the total sampled air volume, and  $f$  is the fraction of filter  
 184 that was used in the extraction.

185 For comparison of ice nucleation activity of the different dust events, the INP concentration in the liquid was converted to the  
186 number of active sites per unit surface area of INPs, i.e., the surface density of sites  $n_s$ , active above temperature,  $T$  (Vali,  
187 1971):

$$188 \quad n_s(T) = \frac{-\ln(1-f_{ice}(T))}{A} \quad [m^{-2}] \quad (3),$$

189 where  $A$  is the surface area immersed in a single droplet of the experiment, based on the total surface area of particles in the  
190 suspension.

## 191 **2.8 Scanning Electron Microscopy**

192 A quarter of selected filters were coated with Iridium for analysing the chemical composition of airborne particles using a  
193 scanning electron microscope (SEM; Supra 55VP, LEO) equipped with an Energy-dispersive X-ray spectroscopy (EDX)  
194 detector for elemental microanalysis. The analysis was done at a voltage of 5 kV using the Quantax software (Bruker).

## 195 **3 Results and Discussion**

### 196 **3.1 Air mass Back Trajectories and the Origin of the Dust Storms**

197 The density of air mass back trajectories for 72-h period prior to the sampling for all events are shown in Figure 2. The sampling  
198 site and the surrounding main deserts are shown as well. During the sampled events, the air mass trajectories were diverse. In  
199 some cases, the air masses travelled directly to the sampling site from the source region, while in other cases, they travelled  
200 longer distance. In most events, the air mass had either easterly or westerly component, and were often concentrated in the  
201 same geographical area.

202 The dust origins were identified based on back trajectory analysis, integrated with reanalysis data of remote sensing of  
203 atmospheric dust. We followed the dust mass concentration prior to the sampling period, as detailed in Figure S1. Locations  
204 that contained high levels of suspended dust and overlapped with the air mass trajectories were identified as the possible  
205 sources of dust. The green contours in Figure 2 represent the assigned dust origin for each sampled event based on the reanalysis  
206 data. Note that in two events, there was no overlap between the dust origin and air mass trajectories. These events will be  
207 further discussed below. Two events, denoted by SDS1 and SDS2, originated in North Sahara Desert. The source of SDS1 was  
208 near the border of Egypt and Libya, and the source of SDS2 was in Egypt, east of SDS1. The dust travelled over the  
209 Mediterranean Sea and was potentially affected by the marine environment, possibly obtaining a sea salt or anthropogenic  
210 sulfate coating (Levin et al., 1996). Two other events, denoted by SyDS1 and SyDS2, originated from the Syrian Desert, from  
211 western Iraq and southern Syria. Compared to the Saharan events, the dust mass density in the Syrian Desert events was  
212 relatively low.

213 Another event was defined as a “mixed dust” event (MDS), because it was more complicated and included contributions of  
214 different sources: the analysis indicates that there is one possible dust origin east of the sampling site in the Syrian Desert, and

215 another one southwest of the sampling site in the Sahara Desert. However, the air mass trajectories did not overlap with the  
216 Saharan dust origin, but indicated that the air mass was transported from the Red Sea. Further analysis of the air mass  
217 trajectories prior to the sampling period in the Red Sea showed that both Sahara and Arabia dusts were transported to the Red  
218 Sea (see the supplementary part, Figure S2(a)). Another event did not show overlap between the air mass trajectories and the  
219 dust origin. Further analysis of air mass back trajectories in the days prior to the sampling period showed that dust was  
220 transported to the Mediterranean Sea from the region of Libya in the Sahara Desert, towards Turkey, and was deflected  
221 eastward by westerly winds to the sampling site (see the supplementary part, Figure S2(b)). The dusty air masses rapidly  
222 cleared up, and relatively non-dusty air masses arrived at the sampling site, as inferred from  $PM_{10}$  concentrations and the OPC  
223 size distributions, see section 3.2. This event was defined as “clean and Saharan dust storm” and denoted by CSDS. Table 1  
224 summarizes the sampled events, their sampling periods, and the peak and mean  $PM_{10}$  concentrations during sampling. Peak  
225 values ranged from  $67 \mu\text{g m}^{-3}$  in CSDS and  $132 \mu\text{g m}^{-3}$  in SyDS1, to  $717 \mu\text{g m}^{-3}$  in SDS2, which was the strongest dust event  
226 in this study. In SDS1, MDS and SyDS2, the values ranged between  $\sim 300$  to  $400 \mu\text{g m}^{-3}$ . When comparing the mean  $PM_{10}$   
227 concentrations during the entire sampling periods, CSDS was categorized as a non-dusty event, with the lowest concentrations  
228 of  $30 \pm 13 \mu\text{g m}^{-3}$ , i.e. below the threshold of  $42 \mu\text{g m}^{-3}$  for dusty conditions (Krasnov et al., 2014). The mean values in the rest  
229 of the events ranged from 76 to  $206 \mu\text{g m}^{-3}$ , and were therefore categorized as dust storms.

### 230 **3.2 Particle Number-Size Distributions**

231 Figure 3(a) describes the mean particle number-size distributions of sampled air during the dust events, as was detected by the  
232 GRIMM OPC. The lowest channel of the GRIMM includes particles that are larger than  $0.25 \mu\text{m}$ . This channel possibly  
233 underestimates the total particle count since the counting efficiency is less than 100%.

234 The number-size distributions had similar patterns in all the events. The highest particle number concentrations were in the  
235 submicron size range, decreasing towards larger particles. Events SDS1, SDS2, and MDS had a rather similar particle  
236 concentration distribution. Event SyDS1 showed similar particle concentrations in the submicron range, but the particle  
237 concentrations in the supermicron range were about an order of magnitude lower, which was also apparent in the  $PM_{10}$  data.  
238 CSDS, a predominantly non-dusty event, had the lowest particle concentrations in comparison to the rest of the sampled events,  
239 as was also indicated by the  $PM_{10}$  data. In the SyDS2 event, exceptionally high concentrations in the supermicron range above  
240  $3 \mu\text{m}$  were observed, and the peak extended towards larger particle sizes, combined with relatively high particle concentrations.  
241 Note that prior to and during this event, a series of biomass burning events occurred in Israel extending to about 100 km north  
242 and 50 km east of the sampling site. Therefore, this peak may include also contributions from biomass burning particles. This  
243 is further supported by the SEM-EDX analysis of the filters from this event, which in comparison with the other events,  
244 contained super-aggregates in the supermicron range, typically observed in biomass burning emissions (Chakrabarty et al.,  
245 2014), with distinct morphologies and elemental composition (shown in the supplementary part in Figure S3).

246 The surface-area-size distributions shown in Figure 3(b) compare the contribution of supermicron and submicron particles to  
247 the available ambient surface area. Ice nucleation initiated on the surface of the particles, and therefore, their surface area  
248 concentration is an important parameter in addition to number concentrations. Here it is clearly seen that the potential  
249 contribution of the supermicron particles to the ice nucleation may be significant when compared to the submicron particles,  
250 although their number concentrations were up to two orders of magnitude lower.

### 251 **3.3 Airborne INP Concentrations**

252 The cumulative INP concentration spectra for the six dust events are shown in Figure 4. In each event, different particle size  
253 classes are marked by different color. Freezing was observed between 255 and 238 K, and the INP concentrations spanned  
254 four orders of magnitude from  $10^{-1}$  to  $10^3$  L<sup>-1</sup> of air.

255 A particle size dependence of the freezing temperature and INP concentration was observed. Larger particles froze at warmer  
256 temperatures with higher number of INPs. The variation between the six size-classes ranged from 1 to 2 orders of magnitude,  
257 and in some cases the smallest particles had similar behavior to the large ones. For example, in event SDS2, size-classes  
258  $D_{50}=0.6$   $\mu\text{m}$  and  $D_{50}=0.3$   $\mu\text{m}$  were less ice-active than the rest of the size-classes, while in MDS, all size classes showed similar  
259 activity. As an exception, event SyDS2 showed a weaker size dependence in comparison to the other dust events, and in some  
260 size-classes, lower INP concentrations. In comparison, in the relatively non-dusty event CSDS, the variability between the  
261 different size classes was higher, especially at lower temperatures. In Figure 5, similarly to Figure 4, INP concentrations are  
262 presented, but arranged according to the different size classes. The variability within each size class was relatively high and  
263 spans over 2 orders of magnitude; for example, at size class  $D_{50}=0.3$   $\mu\text{m}$  near 245 K, INP concentration ranged from about 1  
264 to almost  $10^2$  L<sup>-1</sup> of air. It is clearly seen that INP concentrations in dusty conditions (SDS1, SDS2, MDS and SyDS1) were  
265 higher than in non-dusty conditions (CSDS) for the supermicron range, but similar in the submicron range. Previous studies  
266 also pointed out the significant contribution of supermicron particles to the INP population. Mason et al. (2016) studied the  
267 immersion freezing abilities of airborne particles in North America and Europe, and found that supermicron particles  
268 dominated the freezing, especially at relatively high temperature (258 K). Recent measurements in a coastal tropical site  
269 conducted by Ladino et al. (2019) also found high concentrations of INPs at relatively high temperatures ( $> 258$  K) due to  
270 supermicron particles. In these studies, however, mineral dust is not expected to dominate the samples, and bioaerosol particles  
271 are thought to dominate the freezing at the high temperatures ( $> 258$  K). At lower temperatures (below 253 K), Ladino et al.  
272 (2019) suggested that mineral dust dominated the freezing. Moreover, DeMott et al. (2010) found that INP concentrations are  
273 correlated with particles  $> 0.5$   $\mu\text{m}$ . Other studies, such as Rosinski et al. (1986) and Huffman et al. (2013), also found that  
274 supermicron particles were responsible for most of the INP population in some cases, while when changing the freezing mode  
275 that was analysed or the measurement meteorological conditions, their contribution was reduced. Vali (1966) in contrast, found  
276 that submicron particles dominate freezing in hail melt samples.

### 277 3.4 Size-Dependence of Ice Active Site Density ( $n_s(T)$ )

278 Figure 6 presents the  $n_s(T)$  curves for the different dust events spanning a range of  $10^6 \text{ m}^{-2}$  at 253K to  $10^{11} \text{ m}^{-2}$  at 238 K. In  
279 general,  $n_s(T)$  increased with particle size. The highest  $n_s$  values were observed in the supermicron range  $D_{50}=5.6 \text{ }\mu\text{m}$ ,  
280 followed by  $D_{50}=3.2$ , 1.8 and  $1.0 \text{ }\mu\text{m}$ . The activity of the latter three classes was similar within measurement uncertainties. In  
281 the submicron range, stages  $D_{50}=0.6$  and  $0.3 \text{ }\mu\text{m}$ , the  $n_s(T)$  values were lower than in the supermicron range and showed  
282 higher variability between the different events, except for the MDS event, that had similar activity in the submicron and the  
283 supermicron range. While INP concentrations may generally vary due to experimental parameters, such as particle  
284 concentration in the droplet or droplet size,  $n_s(T)$  accounts for these differences since it is normalized by the total surface area  
285 of particles immersed in the droplet. Therefore, the effect of particle size diminishes using the  $n_s(T)$  curves, if the particles'  
286 ice-nucleation ability is indeed similar. Hence, the analysis presented in Figure 6 indicates that the supermicron particles are  
287 better INP than the submicron ones, implying they have more active sites or/and active sites that nucleate ice at higher  
288 temperatures.

289 Figure 7 displays the same  $n_s(T)$  curves as Figure 6, but now arranged according to the different size-classes. It is observed  
290 that in the supermicron range, all  $n_s(T)$  curves from the different events merge (with the exception of SyDS2) suggesting that  
291 freezing was dominated by a common component. While the freezing activity decreases with decreasing particle size, the  
292 shape of the curves is preserved, suggesting that the abundance of this common component decreases with particle size. One  
293 possible explanation for this observation may be mineralogy segregation, known to occur with particle size: larger particles  
294 contain more primary minerals, such as K-feldspar, whereas smaller particles contain more secondary minerals, such as clays  
295 and quartz that are common in all particle sizes (Perlwitz et al., 2015; Claquin et al., 1999). Therefore, the reduced activity in  
296 the submicron range and the higher variability between the dust events, especially at  $D_{50}=0.3 \text{ }\mu\text{m}$ , may be attributed to a  
297 different mineralogical composition of the particles, or to the lack of the important ice-inducing component. Alternatively, it  
298 is also possible that the submicron particles are mixed with other particle types, that are more common in this size range, such  
299 as urban pollution (Weijun et al., 2016), and therefore freezing may not be dominated exclusively by mineral dust. Moreover,  
300 due to their larger surface-to-volume ratio, submicron particles are more sensitive to atmospheric processing than supermicron  
301 particles, which can lead to further deactivation of their ice active sites (Boose et al., 2016a). These considerations may explain  
302 the variability in the activity between different events. For example, we propose that the passage of SDS1 and SDS2 over the  
303 Mediterranean Sea can contribute to their reduced activity in the submicron range, while for the MDS event, a shorter and  
304 relatively direct transport path resulted in less atmospheric processing. Although speculative, these considerations may  
305 possibly explain why the freezing activity of submicron particles converged with those of the supermicron particles, but we  
306 acknowledge that further measurements are needed to confirm these suggestions.

307 In Figure 7, we also compare a few relevant  $n_s(T)$  curves of standard minerals, as derived by Atkinson et al. (2013) and  
308 Niedermeier et al. (2015), together with our measured  $n_s(T)$  curves. The standard curves of K-, Na/Ca-feldspar and quartz  
309 were scaled to the estimated fraction of these minerals in AMD (see Table S1), and are typically used for prediction of AMD

310 ice nucleating activity. A good agreement of the absolute  $n_s$  values was observed in the relevant temperature range, and the  
311 slopes of the curves were similar to those of the feldspars, especially for the supermicron range. A good agreement was also  
312 observed with the standard  $n_s(T)$  curve of quartz, suggesting that it contributes to freezing of the submicron particles in the  
313 lower temperature range. Note that the standard  $n_s(T)$  curves of clay minerals and calcite were not plotted here despite their  
314 large abundance in AMD, because there was no overlap with the ice nucleation activity in this study. Only the freezing activity  
315 of the largest particles ( $D_{50}=5.6 \mu\text{m}$ ) overlapped with the K-feldspar prediction of Atkinson et al. (2013), indicating that this  
316 prediction possibly overestimates the freezing activity of the entire size distribution of AMD. For the particles in the size range  
317 of  $3.2 < D_{50} < 1.0 \mu\text{m}$ , there is an overlap in activity with the K-feldspar prediction of Niedermeier et al. (2015) and Na/Ca-  
318 feldspar of Atkinson et al. (2013). However, in all cases, the feldspars predictions overestimate the freezing activity of AMD  
319 in the submicron range.

320 The  $n_s(T)$  curves of SyDS2 displays moderate slopes and lower IN activity in comparison with the other dust events, in all  
321 size classes, except for the smallest particles with  $D_{50}=0.3 \mu\text{m}$ . As was already mentioned, these particles were most likely  
322 mixed with smoke particles from biomass-burning events that occurred during the same period, and the filters from this event  
323 were covered with super-aggregate particles in the supermicron size, rich with potassium, similar to particles seen in other  
324 biomass burning events (Chakrabarty et al., 2014).

### 325 **3.5 Comparison of WISDOM and BINARY measurements for event CSDS**

326 A complementary analysis for the CSDS event using BINARY is shown in Figure 8. BINARY probes droplets with larger  
327 volumes and, thus, it is more sensitive to less common ice-nucleating sites that may not show a signal in WISDOM. In the  
328 BINARY experiments, two suspensions were tested, with different dilution factors, for extending our sensitivity. The higher  
329 total dust surface area per droplet sample that was investigated in the BINARY experiments, yellow markers in Figure 8,  
330 demonstrates the warmest freezing temperatures, ranging from 255 to 246 K, and the  $n_s(T)$  values ranged from  $10^6$  to  $10^9 \text{ m}^{-2}$ .  
331 The 1:10 diluted samples (purple markers) showed freezing at lower temperatures, ranging from about 251 to 244 K, with  
332 higher  $n_s(T)$  values ranging from  $10^8$  to  $10^{11} \text{ m}^{-2}$ . In some of the dilute cases of the BINARY experiments, the data were at  
333 the limit of the background impurities (see supplementary part, Figure S5). In order to include only data that are significantly  
334 different from the background, a criterion was set, in which only those data points that are larger by at least two standard  
335 deviations than the mean background impurities were further considered in Figure 8. If data were below that threshold, they  
336 were considered as not significant and thus were removed (e.g., the data of the  $D_{50}=0.6$  and  $0.3 \mu\text{m}$  for the diluted BINARY  
337 samples).

338 Figure 8 shows a very good agreement between the BINARY and WISDOM data, because the  $n_s(T)$  curves merged nicely  
339 onto each other for each size-class. Whereas BINARY was more sensitive than WISDOM to the warmer and relatively rare  
340 active sites, WISDOM detected the more common active sites in the low temperature range. Overall, the dependence of the  
341 freezing activity temperature range on the immersed surface area per droplet is well demonstrated here, where a reduction in

342 the surface area of the different experiments (WISDOM < BINARY diluted < BINARY) decreased the probability to observe  
343 freezing at the higher temperatures. This was also demonstrated previously in studies of standard mineral dust (Broadley et al.,  
344 2012;Marcolli et al., 2007;Reicher et al., 2018). Overall, the data shown in Figure 8 indicate the added value when using  
345 experimental techniques of different sensitivity for the purpose of measuring the concentration and active site density of INP  
346 in field studies (e.g., Atkinson et al. (2013); Chen et al. (2018);Harrison et al. (2018)).

347

### 348 **3.6 Comparison of Super- and Submicron ranges with AMD Measurements and Predictions**

349 The particle surface area that was used to derive  $n_s(T)$  represents the total airborne particles that were collected for each  
350 sample, regardless of particle composition. When mineral dust dominated the composition, as in a dust event case (see for  
351 example Figure S4 in the supplementary part), we treat  $n_s(T)$  as representative for AMD freezing. Figure 9(a) compiles the  
352  $n_s(T)$  results of AMD from a few recent studies that focused on airborne particles (albeit not size-selected) during dust events.  
353 Results from our current study, excluding the events SyDS2 and CSDS that were not dominated by AMD, are presented  
354 alongside those of Price et al. (2018) and Boose et al. (2016b). Price et al. (2018) collected airborne particles in flights west of  
355 the Sahara Desert over the tropical Atlantic at altitudes of up to 3.5 km. Boose et al. (2016b) analysed airborne particles which  
356 were deposited in the Eastern Mediterranean region in Egypt, Cyprus and the Peloponnese (Greece) during dust events. Boose  
357 et al. (2016b) also sampled airborne particles during dust events over Tenerife, off West Africa. In addition, we present  
358 measurements which were also conducted in the Eastern Mediterranean region in Cyprus. Schrod et al. (2017) measured INP  
359 in the lower troposphere using an unmanned aircraft system and Gong et al. (2019) measured INP at ground level. Both studies  
360 measured the immersion freezing of the sampled particles during different atmospheric conditions that included few dust  
361 plumes from the Sahara. Note that here we present only immersion/condensation freezing measurements by Schrod et al.  
362 (2017) and not the entire data . Also note that the presented data is not necessarily dominated by mineral dust, in contrast to  
363 the current study or to Price et al. (2018) and Boose et al. (2016b). The specific cases where the samples were taken during  
364 passage of dust plumes and are possibly dominated by mineral dust are marked in Figure 9(a) in green for Schrod et al. (2017)  
365 and cyan for Gong et al. (2019). The supermicron data presented in this paper is about 1 to 2 orders of magnitude higher, while  
366 our submicron data is in relatively good agreement with Schrod et al. (2017), except for the lowest temperature (243 K) points  
367 where 1 to 3 orders of magnitude differences were observed. The Gong et al. (2019) data are lower in 1 to 3 orders of magnitude  
368 but there is some overlapping with this study and with Price et al. (2018).

369 This compilation of the data that was dominated by mineral dust (i.e., this study, Price et al. (2018) and Boose et al. (2016b))  
370 shows that  $n_s(T)$  curves from the different studies exhibit great similarities over a wide range of temperatures (236 - 265 K)  
371 for dust from different locations and geographic sources, with varying atmospheric paths and altitudes. This similarity may  
372 have significant implications for modelling ice nucleation activity by AMD, since it suggests that parameterizations can be  
373 simplified, for example by neglecting the complication of accounting for mineralogy of different geographical sources. Due



374 to the different behaviour of submicron and supermicron particles, we also suggest that accounting for the particle size class  
375 will improve the prediction of ice cloud formation. For that purpose, we derived two basic parameterizations (Eq.4), for  
376 supermicron and submicron particles, based on the combined AMD data (including data from this study, Price et al. (2018)  
377 and Boose et al. (2016b), and excluding SyDS2), which cover a wide range of temperatures, and spread more than 5 orders of  
378 magnitudes in  $n_s(T)$  values. These parameterizations are the best mathematical fit for a Hill-type equation, which is normally  
379 used for fitting S-shaped data as they are observed in this compilation:

$$380 \quad n_s(T) = \exp[y_0 + a/(b + \exp[(T - 248)/c])] [m^{-2}] \quad (4)$$

381 where the coefficients (95% confidence bounds) for supermicron range particles are set to:

$$382 \quad y_0 = 11.47 \quad (10.97, 11.98), a = 24.00 \quad (22.01, 25.99), b = 1.53 \quad (1.35, 1.70), \text{ and } c = 4.54 \quad (4.06, 5.02),$$

$$383 \quad T \in [236K, 266K] \quad (R^2 = 0.93).$$

384 and for submicron range:

$$385 \quad y_0 = 9.48 \quad (8.19, 10.76), a = 23.00 \quad (20.23, 25.77), b = 1.34 \quad (1.10, 1.57), \text{ and } c = 7.38 \quad (5.84, 8.92),$$

$$386 \quad T \in [238K, 266K] \quad (R^2 = 0.93).$$

387 Parameterizations for each individual size class can be found in Table S2 in the supplementary part.

388 In Figure 9(b), the parameterizations derived here are presented next to the recent parameterizations of ice nucleation of desert  
389 dust by Ullrich et al. (2017) and Niemand et al. (2012). These parameterizations are based predominantly on natural surface-  
390 collected dust samples, but also contained one sample of AMD from Israel, and agrees within an order of magnitude with our  
391 supermicron data in the low-temperature range (243 - 247 K), but overpredicts  $n_s(T)$  by more than an order of magnitude  
392 when compared to our submicron data and to the Price et al. (2018) data at warmer temperatures (247-259 K). This emphasizes  
393 that AMD ice nucleation may not be correctly represented when based on desert dust sampled from the surface, consistent  
394 with the conclusions of Boose et al. (2016b) who showed that the average freezing activity of AMD is reduced when compared  
395 to the activity of surface-collected desert dust. K-feldspar parameterizations by Atkinson et al. (2013) and Niedermeier et al.  
396 (2015) are also shown here, and as mentioned before, overpredicts the freezing activity of AMD at temperatures lower than  
397 about 255 K.

## 398 4 Conclusions

399 We characterized the INP activity of particles collected during several mineral dust events in the Eastern Mediterranean. Dust  
400 from the Sahara Desert, the major source for atmospheric dust, together with dust from the Arabian and Syrian deserts were  
401 included. Six size classes were studied that cover both the super- and submicron size ranges. The INP concentrations ranged  
402 from  $10^{-1} \text{ L}^{-1}$  of air in the relatively weak dust events to  $10^3 \text{ L}^{-1}$  of air in the strongest event. The  $n_s$  values ranged from  $10^6$  to  
403  $10^{11} \text{ m}^{-2}$  in the temperature range of 238 – 255 K. A size dependence was observed, both in the INP concentration and in  $n_s$   
404 values. Larger particles were more active INP, exhibited higher INP concentrations and a higher number of nucleating sites  
405 per surface area at higher temperatures. Comparison between freezing results of WISDOM with BINARY showed good

406 agreement, strengthened previous studies that observed how the freezing activity could depend on technical properties and  
407 limitations of the used instrumentation, and therefore emphasize the importance of using complementary instruments.  
408 The dust events studied here represent a range of dust loads, different dust origins and atmospheric paths. Yet, the supermicron  
409 particles in these events exhibited similar freezing abilities. This may indicate that there is a unique component that is  
410 responsible for freezing activity, as was previously suggested (Atkinson et al., 2013;Boose et al., 2016b;Kaufmann et al.,  
411 2016;Price et al., 2018). Our measurements showed that the activity of the supermicron particles was in the range of standard  
412 particles of feldspar mineral, and that the activity of the submicron particles was in the range of standard quartz. Therefore,  
413 we suggest that these may be the two most important components that dominate the freezing by atmospheric mineral dust  
414 (AMD), and therefore may be important for heterogeneous ice nucleation in atmospheric clouds. The submicron particles  
415 showed higher variability between events, possibly due to different composition of the particles or higher sensitivity to  
416 atmospheric processing during long-range transport. In general, supermicron particles contributed the most to the INP  
417 concentration, in agreement with other previous studies (Mason et al., 2016;Huffman et al., 2013;Ladino et al., 2019).  
418 However, our current study is probably the only case where mineral dust dominated the samples. Nevertheless, all of these  
419 studies highlight the importance of the supermicron size class of AMD for atmospheric ice nucleation.  
420 Mineral dust is important both on a regional scale, near its source region, and on a global scale, since it remains ice-active even  
421 after long transport in the atmosphere and thus over considerable distances (DeMott et al., 2003b;Chou et al., 2011). With the  
422 distance from the dust source, supermicron particles will settle, and submicron particles may then dominate ice nucleation on  
423 the global scale (Ryder et al., 2013;Murray et al., 2012). However, recent airborne measurements found coarse and giant  
424 particles in the vicinity and also far from source regions (Ryder et al., 2018). Therefore, including the particle size class in INP  
425 parameterizations can improve predictions of ice formation in clouds. Moreover, information on airborne INP size distributions  
426 may be helpful in identifying the dominant INP sources (Mason et al., 2016). The overprediction of AMD freezing ability  
427 demonstrated in this study, by the Atkinson et al. (2013), Niedermeier et al. (2015);Niemand et al. (2012) and Ullrich et al.  
428 (2017) parameterizations, especially for submicron particles, emphasizes the importance of future studies to better quantify  
429 the changes in the ice-nucleating properties of AMD by atmospheric processing.

430

431

432 **Data availability.** Data are available upon request to the first author.

433

434 **Author contributions.** NR and YR designed the experiments, carried out the field measurements, conducted freezing  
435 experiments in WISDOM, and wrote the paper. CB, LE and TK designed and performed freezing experiments in BINARY.  
436 SRR performed backtrajectory analyses. NR and IKA performed the chemical analyses of filters. All authors contributed to  
437 the discussion and analysis of data and the writing of the manuscript.

438

439 **Competing interests.** The authors declare that they have no conflict of interest.

#### 440 **Acknowledgments**

441 This study was partially funded by the Israel Science Foundation (grant #236/16). The authors are grateful for funding by the  
442 German Research Foundation (DFG) through the research unit FOR 1525 (INUIT) under KO 2944/2-2 for C.B. and T.K., and  
443 a Mercator Fellowship for Y.R., and acknowledge the support from The Helen Kimmel Center for Planetary Sciences, and the  
444 de Botton Center for Marine Sciences. Analyses and visualizations of MERRA data in this study were produced with the  
445 Giovanni online data system, developed and maintained by the NASA GES DISC (<http://giovanni.sci.gsfc.nasa.gov/Giovanni>),  
446 PM<sub>10</sub> data is available from the Israel Ministry of Environmental Protection website  
447 (<http://www.svivaqam.net/Default.rtl.aspx>). Other data used in this study can be retrieved from [osf.io/gpuqt](http://osf.io/gpuqt).

#### 448 **References**

449 Anderson, B., and Hallett, J.: Supersaturation and time dependence of ice nucleation from the vapor on single crystal  
450 substrates, *Journal of the Atmospheric Sciences*, 33, 822-832, 1976.

451 Ansmann, A., Tesche, M., Althausen, D., Müller, D., Seifert, P., Freudenthaler, V., Heese, B., Wiegner, M., Pisani, G.,  
452 Knippertz, P., and Dubovik, O.: Influence of Saharan dust on cloud glaciation in southern Morocco during the Saharan  
453 Mineral Dust Experiment, *Journal of Geophysical Research: Atmospheres*, 113, D04210, 10.1029/2007JD008785, 2008.

454 Archuleta, C. M., DeMott, P., and Kreidenweis, S.: Ice nucleation by surrogates for atmospheric mineral dust and mineral  
455 dust/sulfate particles at cirrus temperatures, *Atmospheric Chemistry and Physics*, 5, 2617-2634, 2005.

456 Ardon-Dryer, K., and Levin, Z.: Ground-based measurements of immersion freezing in the eastern Mediterranean,  
457 *Atmospheric Chemistry and Physics*, 14, 5217-5231, 2014.

458 Atkinson, J. D., Murray, B. J., Woodhouse, M. T., Whale, T. F., Baustian, K. J., Carslaw, K. S., Dobbie, S., O'Sullivan, D.,  
459 and Malkin, T. L.: The importance of feldspar for ice nucleation by mineral dust in mixed-phase clouds, *Nature*, 498, 355-  
460 358, 10.1038/nature12278, 2013.

461 Augustin-Bauditz, S., Wex, H., Kanter, S., Ebert, M., Niedermeier, D., Stolz, F., Prager, A., and Stratmann, F.: The  
462 immersion mode ice nucleation behavior of mineral dusts: A comparison of different pure and surface modified dusts,  
463 *Geophysical Research Letters*, 41, 7375-7382, 2014.

464 Ben-Ami, Y., Koren, I., Rudich, Y., Artaxo, P., Martin, S. T., and Andreae, M. O.: Transport of North African dust from the  
465 Bodélé depression to the Amazon Basin: a case study, *Atmospheric Chemistry and Physics*, 10, 7533-7544, 10.5194/acp-10-  
466 7533-2010, 2010.

467 Boose, Y., Sierau, B., García, M. I., Rodríguez, S., Alastuey, A., Linke, C., Schnaiter, M., Kupiszewski, P., Kanji, Z. A., and  
468 Lohmann, U.: Ice nucleating particles in the Saharan Air Layer, *Atmospheric Chemistry and Physics*, 16, 9067-9087, 2016a.

469 Boose, Y., Welti, A., Atkinson, J., Ramelli, F., Danielczok, A., Bingemer, H. G., Plötze, M., Sierau, B., Kanji, Z. A., and  
470 Lohmann, U.: Heterogeneous ice nucleation on dust particles sourced from 9 deserts worldwide—Part 1: Immersion freezing,  
471 *Atmospheric Chemistry and Physics*, 15075-15095, 2016b.

472 Broadley, S. L., Murray, B. J., Herbert, R. J., Atkinson, J. D., Dobbie, S., Malkin, T. L., Condliffe, E., and Neve, L.:  
473 Immersion mode heterogeneous ice nucleation by an illite rich powder representative of atmospheric mineral dust,  
474 *Atmospheric Chemistry and Physics*, 12, 287-307, 10.5194/acp-12-287-2012, 2012.

475 Budke, C., and Koop, T.: BINARY: an optical freezing array for assessing temperature and time dependence of  
476 heterogeneous ice nucleation, *Atmospheric Measurement Techniques*, 8, 689-703, 10.5194/amt-8-689-2015, 2015.

477 Cantrell, W., and Heymsfield, A.: Production of Ice in Tropospheric Clouds: A Review, *Bulletin of the American  
478 Meteorological Society*, 86, 795-807, 10.1175/bams-86-6-795, 2005.

479 Chakrabarty, R. K., Beres, N. D., Moosmüller, H., China, S., Mazzoleni, C., Dubey, M. K., Liu, L., and Mishchenko, M. I.:  
480 Soot superaggregates from flaming wildfires and their direct radiative forcing, *Scientific reports*, 4, 5508, 2014.

481 Chen, J., Pei, X., Wang, H., Chen, J., Zhu, Y., Tang, M., and Wu, Z.: Development, Characterization, and Validation of a  
482 Cold Stage-Based Ice Nucleation Array (PKU-INA), *Atmosphere*, 9, 357, 2018.

483 Chiapello, I., Bergametti, G., Chatenet, B., Dulac, F., Jankowiak, I., Lioussé, C., and Soares, E. S.: Contribution of the  
484 different aerosol species to the aerosol mass load and optical depth over the northeastern tropical Atlantic, *Journal of*  
485 *Geophysical Research: Atmospheres*, 104, 4025-4035, 10.1029/1998JD200044, 1999.

486 Chou, C., Stetzer, O., Weingartner, E., Jurányi, Z., Kanji, Z., and Lohmann, U.: Ice nuclei properties within a Saharan dust  
487 event at the Jungfrauoch in the Swiss Alps, *Atmospheric Chemistry and Physics*, 11, 4725-4738, 2011.

488 Claquin, T., Schulz, M., and Balkanski, Y.: Modeling the mineralogy of atmospheric dust sources, *Journal of Geophysical*  
489 *Research: Atmospheres*, 104, 22243-22256, 1999.

490 Connolly, P., Möhler, O., Field, P., Saathoff, H., Burgess, R., Choularton, T., and Gallagher, M.: Studies of heterogeneous  
491 freezing by three different desert dust samples, *Atmospheric Chemistry and Physics*, 9, 2805-2824, 2009.

492 Cziczo, D., Murphy, D., Hudson, P., and Thomson, D.: Single particle measurements of the chemical composition of cirrus  
493 ice residue during CRYSTAL-FACE, *Journal of Geophysical Research: Atmospheres*, 109, 2004.

494 Cziczo, D. J., Garimella, S., Raddatz, M., Hoehler, K., Schnaiter, M., Saathoff, H., Moehler, O., Abbatt, J. P., and Ladino, L.  
495 A.: Ice nucleation by surrogates of Martian mineral dust: What can we learn about Mars without leaving Earth?, *Journal of*  
496 *Geophysical Research: Planets*, 118, 1945-1954, 2013.

497 Cziczo, D. J., and Froyd, K. D.: Sampling the composition of cirrus ice residuals, *Atmospheric research*, 142, 15-31, 2014.

498 Dayan, U.: Climatology of Back Trajectories from Israel Based on Synoptic Analysis, *Journal of Climate and Applied*  
499 *Meteorology*, 25, 591-595, 10.1175/1520-0450(1986)025<0591:cobtfi>2.0.co;2, 1986.

500 Dayan, U., Heffter, J., Miller, J., and Gutman, G.: Dust intrusion events into the Mediterranean basin, *Journal of Applied*  
501 *Meteorology*, 30, 1185-1199, 1991.

502 Dee, D. P., Uppala, S., Simmons, A., Berrisford, P., Poli, P., Kobayashi, S., Andrae, U., Balmaseda, M., Balsamo, G., and  
503 Bauer, d. P.: The ERA-Interim reanalysis: Configuration and performance of the data assimilation system, *Quarterly Journal*  
504 *of the royal meteorological society*, 137, 553-597, 2011.

505 DeMott, P. J., Cziczo, D., Prenni, A., Murphy, D., Kreidenweis, S., Thomson, D., Borys, R., and Rogers, D.: Measurements  
506 of the concentration and composition of nuclei for cirrus formation, *Proceedings of the National Academy of Sciences*, 100,  
507 14655-14660, 2003a.

508 DeMott, P. J., Sassen, K., Poellot, M. R., Baumgardner, D., Rogers, D. C., Brooks, S. D., Prenni, A. J., and Kreidenweis, S.  
509 M.: African dust aerosols as atmospheric ice nuclei, *Geophysical Research Letters*, 30, n/a-n/a, 10.1029/2003GL017410,  
510 2003b.

511 DeMott, P. J., Prenni, A. J., Liu, X., Kreidenweis, S. M., Petters, M. D., Twohy, C. H., Richardson, M. S., Eidhammer, T.,  
512 and Rogers, D. C.: Predicting global atmospheric ice nuclei distributions and their impacts on climate, *Proceedings of the*  
513 *National Academy of Sciences*, 107, 11217-11222, 10.1073/pnas.0910818107, 2010.

514 Engelbrecht, J. P., McDonald, E. V., Gillies, J. A., “Jay” Jayanty, R., Casuccio, G., and Gertler, A. W.: Characterizing  
515 mineral dusts and other aerosols from the Middle East—Part 2: Grab samples and re-suspensions, *Inhalation toxicology*, 21,  
516 327-336, 2009.

517 Falkovich, A. H., Schkolnik, G., Ganor, E., and Rudich, Y.: Adsorption of organic compounds pertinent to urban  
518 environments onto mineral dust particles, *Journal of Geophysical Research: Atmospheres*, 109, 2004.

519 Fletcher, N.: Active sites and ice crystal nucleation, *Journal of the Atmospheric Sciences*, 26, 1266-1271, 1969.

520 Freedman, M. A.: Potential sites for ice nucleation on aluminosilicate clay minerals and related materials, *The Journal of*  
521 *Physical Chemistry Letters*, 6, 3850-3858, 2015.

522 Ganor, Foner, H. A., Brenner, S., Neeman, E., and Lavi, N.: The chemical composition of aerosols settling in Israel  
523 following dust storms, *Atmospheric Environment. Part A. General Topics*, 25, 2665-2670, [https://doi.org/10.1016/0960-](https://doi.org/10.1016/0960-1686(91)90196-E)  
524 [1686\(91\)90196-E](https://doi.org/10.1016/0960-1686(91)90196-E), 1991.

525 Ganor, E., and Mamane, Y.: Transport of Saharan dust across the eastern Mediterranean, *Atmospheric Environment (1967)*,  
526 16, 581-587, 1982.

527 Ganor, E.: The frequency of Saharan dust episodes over Tel Aviv, Israel, *Atmospheric Environment*, 28, 2867-2871, 1994.

528 Ganor, E., Osetinsky, I., Stupp, A., and Alpert, P.: Increasing trend of African dust, over 49 years, in the eastern  
529 Mediterranean, *Journal of Geophysical Research: Atmospheres*, 115, D07201, 10.1029/2009JD012500, 2010.

530 Garrison, V. H., Shinn, E. A., Foreman, W. T., Griffin, D. W., Holmes, C. W., Kellogg, C. A., Majewski, M. S., Richardson,  
531 L. L., Ritchie, K. B., and Smith, G. W.: African and Asian Dust: From Desert Soils to Coral Reefs, *BioScience*, 53, 469-480,  
532 10.1641/0006-3568(2003)053[0469:AAADFD]2.0.CO;2, 2003.

533 Gat, D., Mazar, Y., Cytryn, E., and Rudich, Y.: Origin-Dependent Variations in the Atmospheric Microbiome Community in  
534 Eastern Mediterranean Dust Storms, *Environmental Science & Technology*, 51, 6709-6718, 10.1021/acs.est.7b00362, 2017.

535 Gelaro, R., McCarty, W., Suárez, M. J., Todling, R., Molod, A., Takacs, L., Randles, C. A., Darmenov, A., Bosilovich, M.  
536 G., and Reichle, R.: The modern-era retrospective analysis for research and applications, version 2 (MERRA-2), *Journal of*  
537 *Climate*, 30, 5419-5454, 2017.

538 Gettelman, A., Liu, X., Barahona, D., Lohmann, U., and Chen, C.: Climate impacts of ice nucleation, *Journal of Geophysical*  
539 *Research: Atmospheres*, 117, 2012.

540 Gong, X., Wex, H., Müller, T., Wiedensohler, A., Höhler, K., Kandler, K., Ma, N., Dietel, B., Schiebel, T., Möhler, O., and  
541 Stratmann, F.: Characterization of aerosol properties at Cyprus, focusing on cloud condensation nuclei and ice nucleating  
542 particles, *Atmospheric Chemistry and Physics Discussion*, 2019, 1-34, 10.5194/acp-2019-198, in review, 2019.

543 Hader, J. D., Wright, T. P., and Petters, M. D.: Contribution of pollen to atmospheric ice nuclei concentrations, *Atmospheric*  
544 *Chemistry and Physics*, 14, 5433-5449, 10.5194/acp-14-5433-2014, 2014.

545 Harrison, A. D., Whale, T. F., Rutledge, R., Lamb, S., Tam, M. D., Porter, G. C., Adams, M. P., McQuaid, J. B., Morris, G.  
546 J., and Murray, B. J.: An instrument for quantifying heterogeneous ice nucleation in multiwell plates using infrared  
547 emissions to detect freezing, *Atmospheric Measurement Techniques*, 11, 5629-5641, 2018.

548 Hoose, C., and Möhler, O.: Heterogeneous ice nucleation on atmospheric aerosols: a review of results from laboratory  
549 experiments, *Atmospheric Chemistry and Physics*, 12, 9817-9854, 10.5194/acp-12-9817-2012, 2012.

550 Huffman, J. A., Prenni, A. J., DeMott, P. J., Pöhlker, C., Mason, R. H., Robinson, N. H., Fröhlich-Nowoisky, J., Tobo, Y.,  
551 Després, V. R., Garcia, E., Gochis, D. J., Harris, E., Müller-Germann, I., Ruzene, C., Schmer, B., Sinha, B., Day, D. A.,  
552 Andreae, M. O., Jimenez, J. L., Gallagher, M., Kreidenweis, S. M., Bertram, A. K., and Pöschl, U.: High concentrations of  
553 biological aerosol particles and ice nuclei during and after rain, *Atmospheric Chemistry and Physics*, 13, 6151-6164,  
554 10.5194/acp-13-6151-2013, 2013.

555 IPCC: IPCC: Climate Change 2013, The Physical Science Basis, Cambridge University Press, Cambridge, United Kingdom  
556 and New York, NY, USA., 2013.

557 Jickells, T. D., An, Z. S., Andersen, K. K., Baker, A. R., Bergametti, G., Brooks, N., Cao, J. J., Boyd, P. W., Duce, R. A.,  
558 Hunter, K. A., Kawahata, H., Kubilay, N., laRoche, J., Liss, P. S., Mahowald, N., Prospero, J. M., Ridgwell, A. J., Tegen, I.,  
559 and Torres, R.: Global Iron Connections Between Desert Dust, Ocean Biogeochemistry, and Climate, *Science*, 308, 67-71,  
560 10.1126/science.1105959, 2005.

561 Kalderon-Asael, B., Erel, Y., Sandler, A., and Dayan, U.: Mineralogical and chemical characterization of suspended  
562 atmospheric particles over the east Mediterranean based on synoptic-scale circulation patterns, *Atmospheric Environment*,  
563 43, 3963-3970, <https://doi.org/10.1016/j.atmosenv.2009.03.057>, 2009.

564 Kandler, K., Benker, N., Bundke, U., Cuevas, E., Ebert, M., Knippertz, P., Rodríguez, S., Schütz, L., and Weinbruch, S.:  
565 Chemical composition and complex refractive index of Saharan Mineral Dust at Izana, Tenerife (Spain) derived by electron  
566 microscopy, *Atmospheric Environment*, 41, 8058-8074, 2007.

567 Kanji, Z. A., Welti, A., Chou, C., Stetzer, O., and Lohmann, U.: Laboratory studies of immersion and deposition mode ice  
568 nucleation of ozone aged mineral dust particles, *Atmospheric Chemistry and Physics*, 13, 9097-9118, 2013.

569 Kanji, Z. A., Ladino, L. A., Wex, H., Boose, Y., Burkert-Kohn, M., Cziczko, D. J., and Krämer, M.: Overview of ice  
570 nucleating particles, *Meteorological Monographs*, 58, 1.1-1.33, 2017.

571 Kaufmann, L., Marcolli, C., Hofer, J., Pinti, V., Hoyle, C. R., and Peter, T.: Ice nucleation efficiency of natural dust samples  
572 in the immersion mode, *Atmospheric Chemistry and Physics*, 16, 11177-11206, 10.5194/acp-16-11177-2016, 2016.

573 Khvorostyanov, V. I., and Curry, J. A.: The theory of ice nucleation by heterogeneous freezing of deliquescent mixed CCN.  
574 Part I: Critical radius, energy, and nucleation rate, *Journal of the Atmospheric Sciences*, 61, 2676-2691, 2004.

575 Kiselev, A., Bachmann, F., Pedevilla, P., Cox, S. J., Michaelides, A., Gerthsen, D., and Leisner, T.: Active sites in  
576 heterogeneous ice nucleation—the example of K-rich feldspars, *Science*, 355, 367-371, 2017.

577 Koop, T., and Murray, B. J.: A physically constrained classical description of the homogeneous nucleation of ice in water,  
578 *The Journal of Chemical Physics*, 145, 211915, 2016.

579 Koren, I., Yoram, J. K., Richard, W., Martin, C. T., Yinon, R., Martins, J. V., and Daniel, R.: The Bodélé depression: a  
580 single spot in the Sahara that provides most of the mineral dust to the Amazon forest, *Environmental Research Letters*, 1,  
581 014005, 2006.

582 Krasnov, H., Katra, I., Koutrakis, P., and Friger, M. D.: Contribution of dust storms to PM10 levels in an urban arid  
583 environment, *Journal of the Air & Waste Management Association*, 64, 89-94, 10.1080/10962247.2013.841599, 2014.

584 Krueger, B. J., Grassian, V. H., Cowin, J. P., and Laskin, A.: Heterogeneous chemistry of individual mineral dust particles  
585 from different dust source regions: the importance of particle mineralogy, *Atmospheric Environment*, 38, 6253-6261, 2004.

586 Ladino, L. A., Raga, G. B., Alvarez-Ospina, H., Andino-Enriquez, M. A., Rosas, I., Martínez, L., Salinas, E., Miranda, J.,  
587 Ramírez-Díaz, Z., and Figueroa, B.: Ice-nucleating particles in a coastal tropical site, *Atmospheric Chemistry and Physics*,  
588 19, 6147-6165, 2019.

589 Laskin, A., Wietsma, T. W., Krueger, B. J., and Grassian, V. H.: Heterogeneous chemistry of individual mineral dust  
590 particles with nitric acid: A combined CCSEM/EDX, ESEM, and ICP-MS study, *Journal of Geophysical Research:*  
591 *Atmospheres*, 110, 2005.

592 Levin, Z., Ganor, E., and Gladstein, V.: The effects of desert particles coated with sulfate on rain formation in the eastern  
593 Mediterranean, *Journal of Applied Meteorology*, 35, 1511-1523, 1996.

594 Li, W., and Shao, L.: Observation of nitrate coatings on atmospheric mineral dust particles, *Atmospheric Chemistry and*  
595 *Physics*, 9, 1863-1871, 2009.

596 Lohmann, U., and Feichter, J.: Global indirect aerosol effects: a review, *Atmospheric Chemistry and Physics*, 5, 715-737,  
597 2005.

598 Lüönd, F., Stetzer, O., Welti, A., and Lohmann, U.: Experimental study on the ice nucleation ability of size-selected  
599 kaolinite particles in the immersion mode, *Journal of Geophysical Research: Atmospheres*, 115, 2010.

600 Mahowald, N., Albani, S., Kok, J. F., Engelstaeder, S., Scanza, R., Ward, D. S., and Flanner, M. G.: The size distribution of  
601 desert dust aerosols and its impact on the Earth system, *Aeolian Research*, 15, 53-71,  
602 <http://dx.doi.org/10.1016/j.aeolia.2013.09.002>, 2014.

603 Marcolli, C., Gedamke, S., Peter, T., and Zobrist, B.: Efficiency of immersion mode ice nucleation on surrogates of mineral  
604 dust, *Atmospheric Chemistry and Physics*, 7, 5081-5091, 10.5194/acp-7-5081-2007, 2007.

605 Marcolli, C.: Deposition nucleation viewed as homogeneous or immersion freezing in pores and cavities, *Atmospheric*  
606 *Chemistry and Physics*, 14, 2071-2104, 2014.

607 Marple, V. A., Rubow, K. L., and Behm, S. M.: A Microorifice Uniform Deposit Impactor (MOUDI): Description,  
608 Calibration, and Use, *Aerosol Science and Technology*, 14, 434-446, 10.1080/02786829108959504, 1991.

609 Mason, R., Si, M., Chou, C., Irish, V., Dickie, R., Elizondo, P., Wong, R., Brintnell, M., Elsasser, M., and Lassar, W.: Size-  
610 resolved measurements of ice-nucleating particles at six locations in North America and one in Europe, *Atmospheric*  
611 *Chemistry and Physics*, 16, 1637-1651, 2016.

612 Mason, R. H., Chou, C., McCluskey, C. S., Levin, E. J. T., Schiller, C. L., Hill, T. C. J., Huffman, J. A., DeMott, P. J., and  
613 Bertram, A. K.: The micro-orifice uniform deposit impactor–droplet freezing technique (MOUDI-DFT) for measuring  
614 concentrations of ice nucleating particles as a function of size: improvements and initial validation, *Atmospheric*  
615 *Measurement Techniques*, 8, 2449-2462, 10.5194/amt-8-2449-2015, 2015.

616 Mazar, Y., Cytryn, E., Erel, Y., and Rudich, Y.: Effect of dust storms on the atmospheric microbiome in the Eastern  
617 Mediterranean, *Environmental Science & Technology*, 50, 4194-4202, 2016.

618 Middleton, N.: Desert dust hazards: A global review, *Aeolian research*, 24, 53-63, 2017.

619 Middleton, N. J., and Goudie, A. S.: Saharan dust: sources and trajectories, *Transactions of the Institute of British*  
620 *Geographers*, 26, 165-181, 10.1111/1475-5661.00013, 2001.

621 Murphy, D., Cziczo, D., Froyd, K., Hudson, P., Matthew, B., Middlebrook, A., Peltier, R., Sullivan, A., Thomson, D., and  
622 Weber, R.: Single-particle mass spectrometry of tropospheric aerosol particles, *Journal of Geophysical Research:*  
623 *Atmospheres*, 111, 2006.

624 Murray, B. J., O'Sullivan, D., Atkinson, J. D., and Webb, M. E.: Ice nucleation by particles immersed in supercooled cloud  
625 droplets, *Chemical Society Reviews*, 41, 6519-6554, 10.1039/C2CS35200A, 2012.

626 Niedermeier, D., Augustin-Bauditz, S., Hartmann, S., Wex, H., Ignatius, K., and Stratmann, F.: Can we define an asymptotic  
627 value for the ice active surface site density for heterogeneous ice nucleation?, *Journal of Geophysical Research:*  
628 *Atmospheres*, 120, 5036-5046, 2015.

629 Niemand, M., Möhler, O., Vogel, B., Vogel, H., Hoose, C., Connolly, P., Klein, H., Bingemer, H., DeMott, P., Skrotzki, J.,  
630 and Leisner, T.: A Particle-Surface-Area-Based Parameterization of Immersion Freezing on Desert Dust Particles, *Journal of*  
631 *the Atmospheric Sciences*, 69, 3077-3092, 10.1175/jas-d-11-0249.1, 2012.

632 O'Sullivan, D., Murray, B. J., Ross, J. F., and Webb, M. E.: The adsorption of fungal ice-nucleating proteins on mineral  
633 dusts: a terrestrial reservoir of atmospheric ice-nucleating particles, *Atmospheric Chemistry and Physics*, 16, 7879-7887,  
634 2016.

635 Perlwitz, J., Pérez García-Pando, C., and Miller, R.: Predicting the mineral composition of dust aerosols–Part 1:  
636 Representing key processes, *Atmospheric Chemistry and Physics*, 15, 11593-11627, 2015.

637 Pratt, K. A., DeMott, P. J., French, J. R., Wang, Z., Westphal, D. L., Heymsfield, A. J., Twohy, C. H., Prenni, A. J., and  
638 Prather, K. A.: In situ detection of biological particles in cloud ice-crystals, *Nature Geoscience*, 2, 398, 2009.

639 Price, H., Baustian, K., McQuaid, J., Blyth, A., Bower, K., Choularton, T., Cotton, R., Cui, Z., Field, P., and Gallagher, M.:  
640 Atmospheric Ice-Nucleating Particles in the Dusty Tropical Atlantic, *Journal of Geophysical Research: Atmospheres*, 123,  
641 2175-2193, 2018.

642 Prospero, J. M.: Long-range transport of mineral dust in the global atmosphere: Impact of African dust on the environment  
643 of the southeastern United States, *Proceedings of the National Academy of Sciences*, 96, 3396-3403, 1999.

644 Pruppacher, H., and Klett, J.: *Microphysics of Clouds and Precipitation: With an Introduction to Cloud Chemistry and Cloud*  
645 *Electricity*, 954 pp, in, Springer, New York, 1997.

646 Reicher, N., Segev, L., and Rudich, Y.: The Weizmann Supercooled Droplets Observation on a Microarray (WISDOM) and  
647 application for ambient dust, *Atmospheric Measurement Techniques*, 11, 233, 2018.

648 Rogers, D. C., DeMott, P. J., Kreidenweis, S. M., and Chen, Y.: Measurements of ice nucleating aerosols during SUCCESS,  
649 *Geophysical Research Letters*, 25, 1383-1386, 1998.

650 Rosenfeld, D., and Woodley, W. L.: Deep convective clouds with sustained supercooled liquid water down to -37.5C,  
651 *Nature*, 405, 440-442, 2000.

652 Rosenfeld, D., Rudich, Y., and Lahav, R.: Desert dust suppressing precipitation: A possible desertification feedback loop  
653 *Proceedings of the National Academy of Sciences*, 98, 5975-5980, 2001.

654 Rosinski, J., Haagenson, P., Nagamoto, C., and Parungo, F.: Ice-forming nuclei of maritime origin, *Journal of Aerosol*  
655 *Science*, 17, 23-46, 1986.

656 Ryder, C., Highwood, E., Lai, T., Sodemann, H., and Marsham, J.: Impact of atmospheric transport on the evolution of  
657 microphysical and optical properties of Saharan dust, *Geophysical Research Letters*, 40, 2433-2438, 2013.

658 Ryder, C. L., Marengo, F., Brooke, J. K., Estelles, V., Cotton, R., Formenti, P., McQuaid, J. B., Price, H. C., Liu, D., Ausset,  
659 P., Rosenberg, P. D., Taylor, J. W., Choularton, T., Bower, K., Coe, H., Gallagher, M., Crosier, J., Lloyd, G., Highwood, E.  
660 J., and Murray, B. J.: Coarse-mode mineral dust size distributions, composition and optical properties from AER-D aircraft  
661 measurements over the tropical eastern Atlantic, *Atmospheric Chemistry and Physics*, 18, 17225-17257, 10.5194/acp-18-  
662 17225-2018, 2018.

663 Sassen, K., DeMott, P. J., Prospero, J. M., and Poellot, M. R.: Saharan dust storms and indirect aerosol effects on clouds:  
664 CRYSTAL-FACE results, *Geophysical Research Letters*, 30, 2003.

665 Schepanski, K.: Transport of mineral dust and its impact on climate, *Geosciences*, 8, 151, 2018.

666 Schrod, J., Weber, D., Drücke, J., Keleshis, C., Pikridas, M., Ebert, M., Cvetković, B., Nickovic, S., Marinou, E., and Baars,  
667 H.: Ice nucleating particles over the Eastern Mediterranean measured by unmanned aircraft systems, *Atmospheric Chemistry*  
668 *and Physics*, 17, 4817, 2017.

669 Spichtinger, P., and Cziczó, D. J.: Impact of heterogeneous ice nuclei on homogeneous freezing events in cirrus clouds,  
670 *Journal of Geophysical Research: Atmospheres*, 115, 2010.

671 Sprenger, M., and Wernli, H.: The LAGRANTO Lagrangian analysis tool–version 2.0, *Geoscientific Model Development*, 8,  
672 2569, 2015.

673 Tan, I., Storelvmo, T., and Zelinka, M. D.: Observational constraints on mixed-phase clouds imply higher climate sensitivity,  
674 *Science*, 352, 224-227, 10.1126/science.aad5300, 2016.

675 Tegen, I., and Fung, I.: Modeling of mineral dust in the atmosphere: Sources, transport, and optical thickness, *Journal of*  
676 *Geophysical Research: Atmospheres*, 99, 22897-22914, 10.1029/94JD01928, 1994.

677 Tunega, D., Gerzabek, M. H., and Lischka, H.: Ab initio molecular dynamics study of a monomolecular water layer on  
678 octahedral and tetrahedral kaolinite surfaces, *The Journal of Physical Chemistry B*, 108, 5930-5936, 2004.

679 Twohy, C., and Poellot, M.: Chemical characteristics of ice residual nuclei in anvil cirrus clouds: evidence for homogeneous  
680 and heterogeneous ice formation, *Atmospheric Chemistry and Physics*, 5, 2289-2297, 2005.

681 Ullrich, R., Hoose, C., Möhler, O., Niemand, M., Wagner, R., Höhler, K., Hiranuma, N., Saathoff, H., and Leisner, T.: A  
682 New Ice Nucleation Active Site Parameterization for Desert Dust and Soot, *Journal of the Atmospheric Sciences*, 74, 699-  
683 717, 10.1175/jas-d-16-0074.1, 2017.

684 Vali, G.: Sizes of atmospheric ice nuclei, *Nature*, 212, 384, 1966.

685 Vali, G.: Quantitative Evaluation of Experimental Results on the Heterogeneous Freezing Nucleation of Supercooled  
686 Liquids, *Journal of the Atmospheric Sciences*, 28, 402-409, 10.1175/1520-0469(1971)028<0402:qeoera>2.0.co;2, 1971.

687 Welti, A., Lohmann, U., and Kanji, Z. A.: Ice nucleation properties of K-feldspar polymorphs and plagioclase feldspars,  
688 *Atmospheric Chemistry and Physics Discussion* <https://doi.org/10.5194/acp-2018-1271>, in review, 2019.

689 Zielke, S. A., Bertram, A. K., and Patey, G.: Simulations of ice nucleation by kaolinite (001) with rigid and flexible surfaces,  
690 *The Journal of Physical Chemistry B*, 120, 1726-1734, 2015.

691 Zimmermann, F., Weinbruch, S., Schütz, L., Hofmann, H., Ebert, M., Kandler, K., and Worringer, A.: Ice nucleation  
692 properties of the most abundant mineral dust phases, *Journal of Geophysical Research: Atmospheres*, 113, 2008.  
693  
694  
695  
696  
697  
698  
699  
700  
701  
702  
703  
704  
705  
706  
707  
708  
709  
710  
711  
712  
713

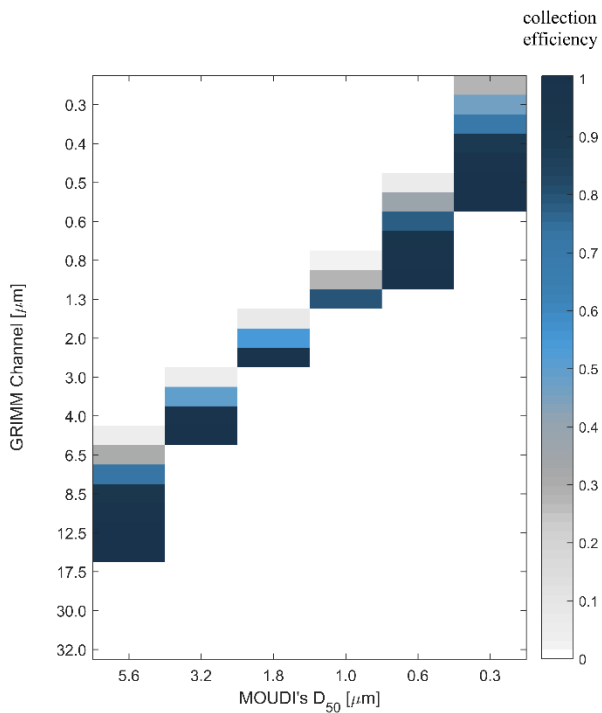


714 **Table 1: Summary of the investigated dust storm events. The events are denoted by their geographic origin: Saharan dust storms**  
 715 **(SDS), Syrian dust storm (SyDS), mixed contribution of the two (MDS), and mix of dust event with a free-dust period (CSDS).**

| Event                            | Start [UTC] | Sampling period [hour] | PM10 peak [ $\mu\text{g m}^{-3}$ ] | PM10 mean [ $\mu\text{g m}^{-3}$ ] | Freezing analysis technique |
|----------------------------------|-------------|------------------------|------------------------------------|------------------------------------|-----------------------------|
| <b>SyDS1</b><br>19 April 2016    | 07:30       | 25                     | 132                                | 76±20                              | WISDOM                      |
| <b>CSDS</b><br>27 April 2016     | 07:30       | 24                     | 67                                 | 30±13                              | WISDOM, BINARY              |
| <b>SyDS2</b><br>23 November 2016 | 15:30       | 18                     | 332                                | 184±68                             | WISDOM                      |
| <b>SDS1</b><br>09 March 2017     | 11:00       | 48                     | 387                                | 96±66                              | WISDOM                      |
| <b>SDS2</b><br>12 March 2017     | 12:00       | 24                     | 717                                | 206±120                            | WISDOM                      |
| <b>MDS</b><br>12 April 2017      | 13:30       | 25                     | 409                                | 141±106                            | WISDOM                      |

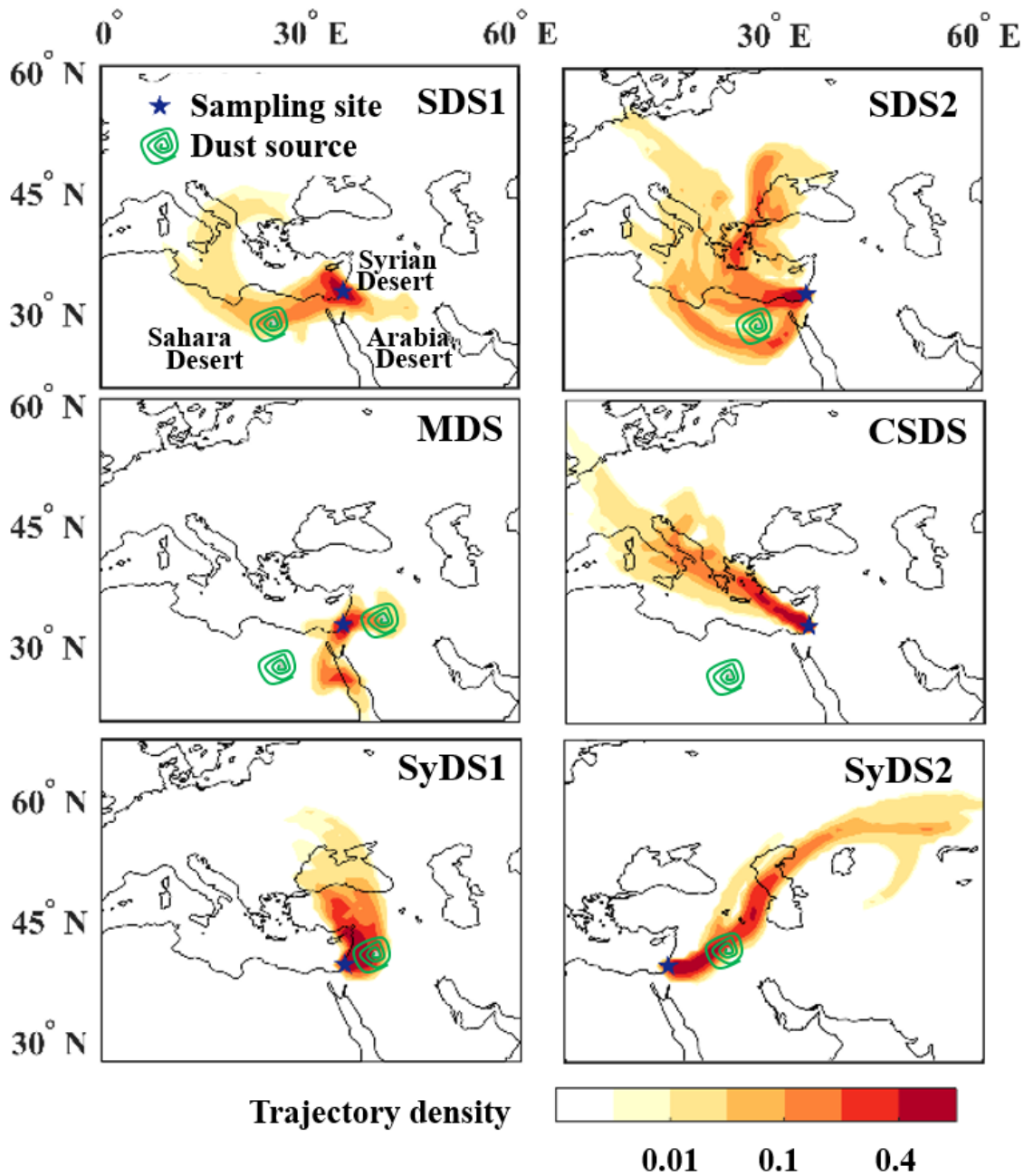
716

717



718

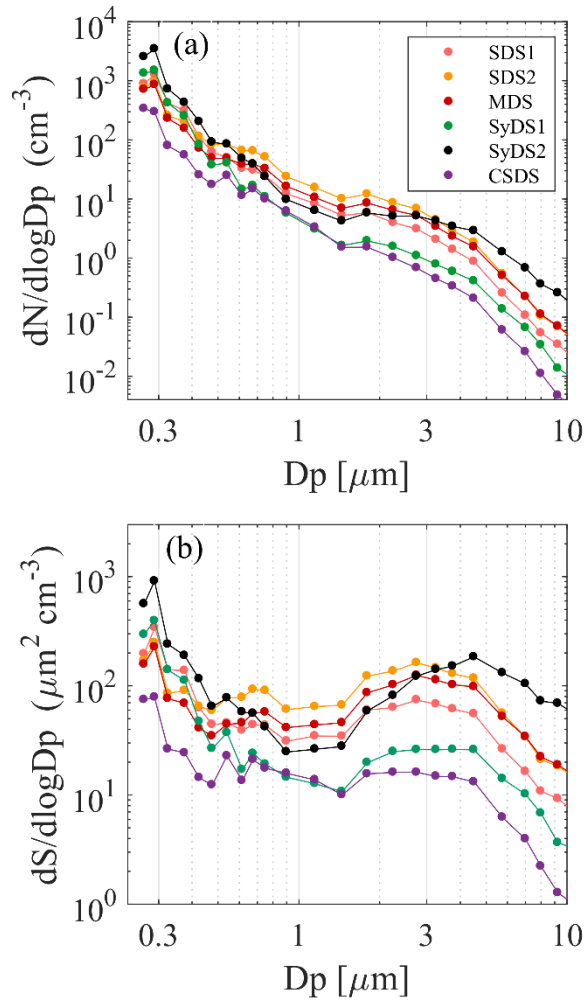
719 **Figure 1: A conversion matrix of GRIMM channels to MOUDI stages. The conversion was based on collection efficiency curves from**  
 720 **Marple et al. (1991). The color shades represent the fraction of particles of a specific GRIMM channel to be impacted on a specific**  
 721 **MOUDI stage.**



722

723 Figure 2: Air mass origin and atmospheric paths of the dust events. Colors represent the density of 72-h backward air mass  
 724 trajectories (normalized to the total trajectory counts). The green contours represent the geographic locations where a high mass of  
 725 the dust occurred during the air mass transition, which is defined as the potential origin of the dust. Abbreviations in the top right of  
 726 each panel indicate the particular dust event.

727



729

730 **Figure 3: Particle size distributions. Particle number size (a) and surface area size (b) distributions averaged over the entire sampling**  
 731 **periods of the events as monitored by GRIMM OPC during the studied events.  $D_p$  is the diameter of the particles and set at the**  
 732 **center of each GRIMM channel.**

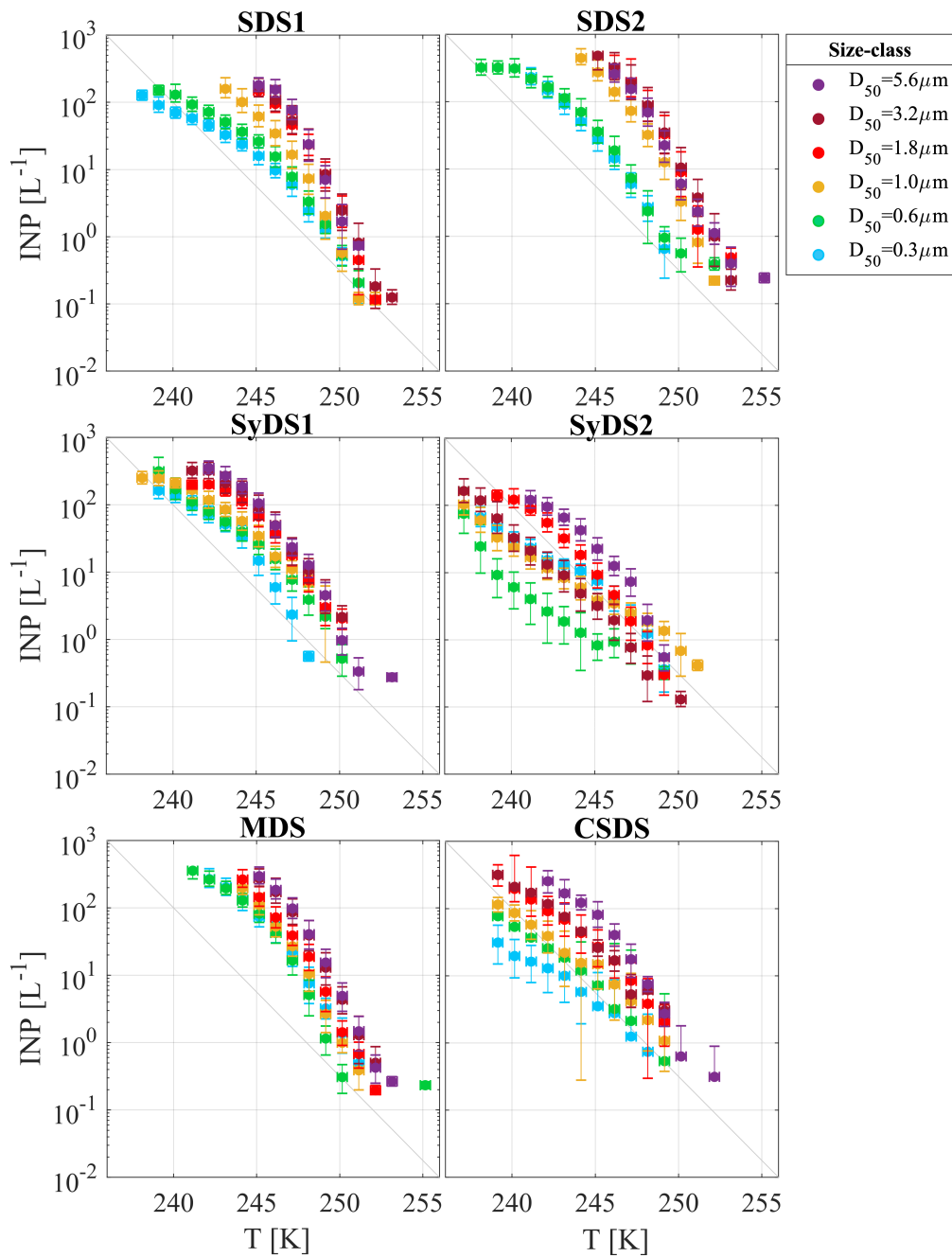
733

734

735

736

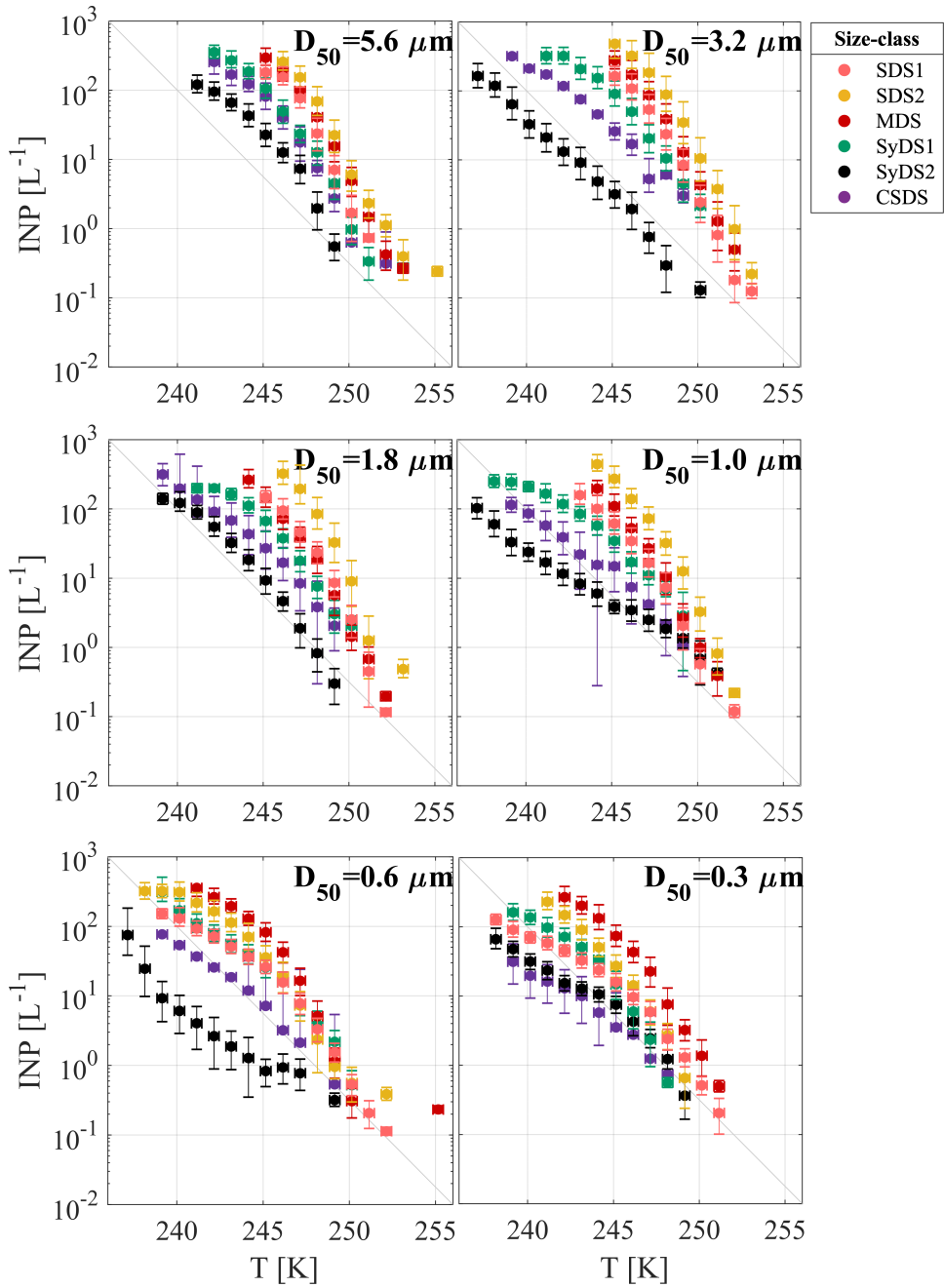
737



738

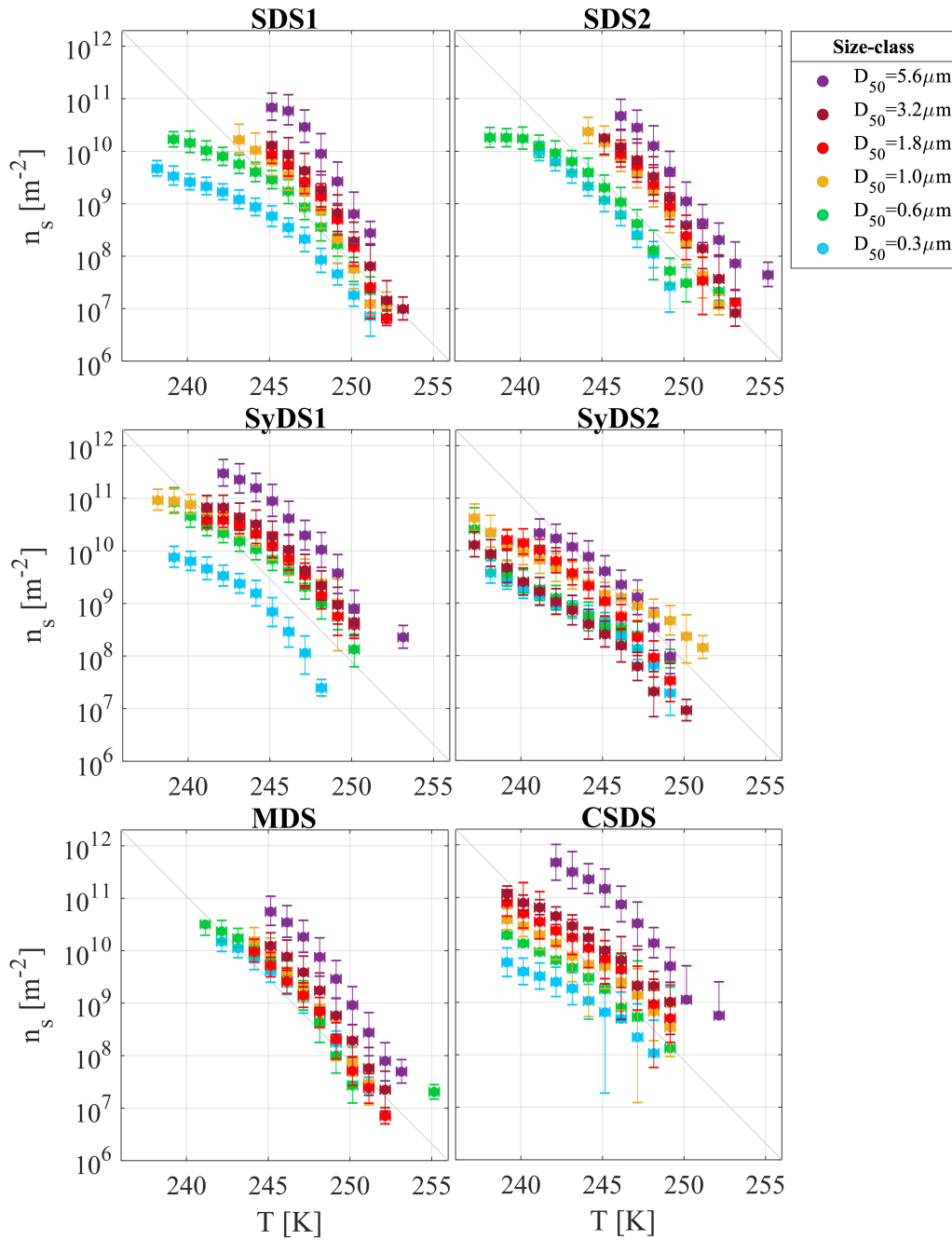
739 **Figure 4: Airborne INP concentrations measured during dust events. INP concentrations per L<sup>-1</sup> air as function of temperature,**  
 740 **presented in different colors for the different particle size-classes. Uncertainty in temperature is 0.3 K. The grey diagonal line is**  
 741 **presented for orientation only.**

742



743

744 **Figure 5: Airborne INP concentrations for various size classes. INP concentrations per L<sup>-1</sup> air as function of temperature, presented**  
 745 **in different colors for the different dust events that were sampled. Uncertainty in temperature is 0.3 K. The grey diagonal line is**  
 746 **presented for orientation only.**



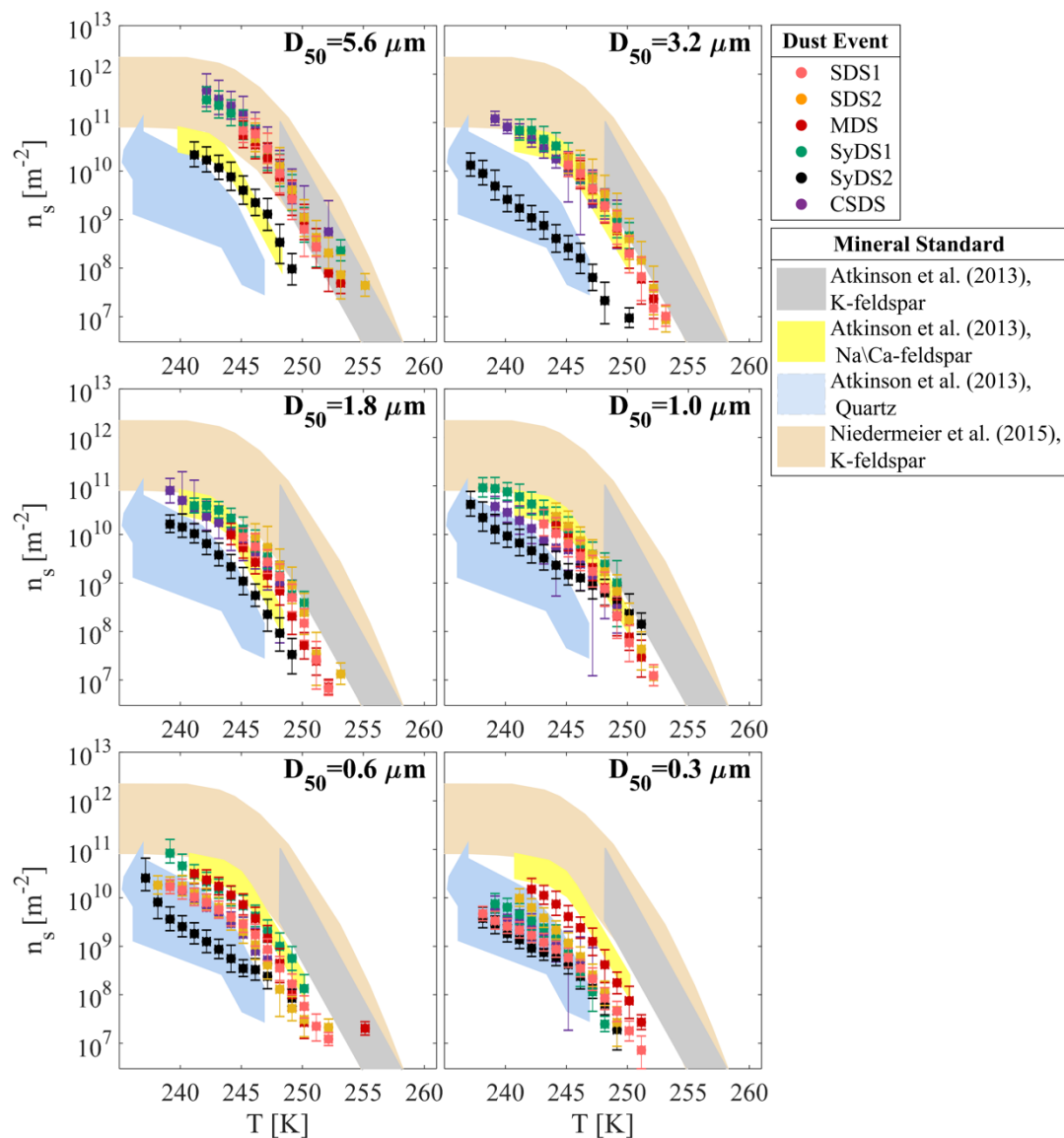
747

748 **Figure 6: Ice active site density as a function of temperature,  $n_s(T)$ , for airborne particles dominated by mineral dust are presented**  
 749 **individually for each dust event. The different colors represent the different size-classes that were investigated. SDS, SyDS and MDS**  
 750 **represent Saharan, Syrian, and mixed dust events, respectively (see text for more details). The linear grey line is identical in each**  
 751 **panel to facilitate comparison.**

752

753

754

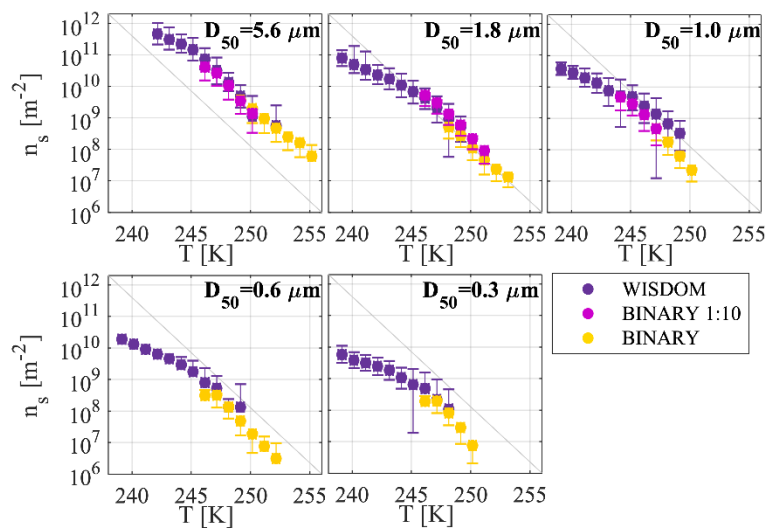


755

756 **Figure 7: Ice active site density during dust events in different particle size classes. Dust events from the Sahara Desert (SDS), Syrian**  
 757 **Desert (SyDS), or both (MDS) are marked by the different colors. Data for  $D_{50} = 3.2, 1.8$  and  $1.0 \mu\text{m}$  of SDS#2 adopted from Reicher**  
 758 **et al. (2018). Relevant standard minerals scaled to ambient values are shown: K-feldspar, Na/Ca-feldspar, and quartz from Atkinson**  
 759 **et al. (2013), and K-feldspar from Niedermeier et al. (2015).**

760

761



762

763 **Figure 8: Complementary measurements of WISDOM and BINARY for CSDS. Analysis in the BINARY was performed to increased**  
 764 **detection sensitivity of ice active site densities. Two suspension with different dilution factors were analysed by BINARY and are**  
 765 **compared here to the WISDOM data for the different size-classes.**

766

767

768

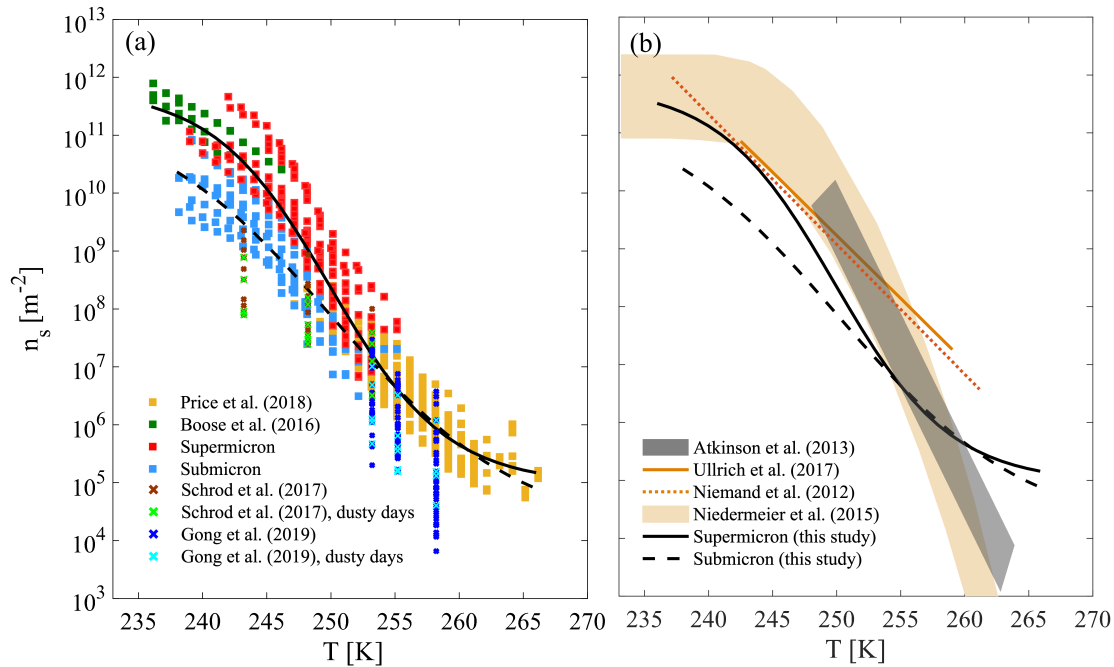
769

770

771

772





773  
 774 **Figure 9: Heterogeneous ice nucleation by airborne particles during dusty conditions.** (a) Active site densities of supermicron and  
 775 submicron size-classes from this study are shown together with flight data (Schrod et al. (2017) and Price et al. (2018)) and deposited  
 776 or *in-situ* data (Boose et al. (2016b) and Gong et al. (2019)). New parameterizations, which were derived in this work based on the  
 777 combined AMD data of the different studies, are shown for supermicron and submicron classes. (b) The new parameterizations  
 778 derived in this study based on all AMD data, shown next to recent parameterizations for desert dust (Ullrich et al. (2017) and  
 779 Niemand et al. (2012)) and K-feldspar predictions (Atkinson et al. (2013) and Niedermeier et al. (2015)).

780

781

782

783

784

785

786